AFRL-AFOSR-VA-TR-2024-0065

Quantification of Atom Probe Tomography Data

Windl, Wolfgang
OHIO STATE UNIVERSITY
1960 KENNY RD
COUMBUS, OH,
US

12/08/2023
Final Technical Report

DISTRIBUTION A: Distribution approved for public release.

Air Force Research Laboratory
Air Force Office of Scientific Research
Arlington, Virginia 22203
Air Force Materiel Command

REPORT DOCUMENTATION PAGE

PLEASE DO NOT RETURN YOUR FORM TO THE ABOVE ORGANIZATION.

1. REPORT DATE	2. REPORT TYPE	3. DATES COVERED	
20231208	Final	START DATE 20190801	END DATE 20230731

4. TITLE AND SUBTITLE
Quantification of Atom Probe Tomography Data

5a. CONTRACT NUMBER	5b. GRANT NUMBER	5c. PROGRAM ELEMENT NUMBER
	FA9550-19-1-0378	61102F
5d. PROJECT NUMBER	**5e. TASK NUMBER**	**5f. WORK UNIT NUMBER**

6. AUTHOR(S)
Wolfgang Windl

7. PERFORMING ORGANIZATION NAME(S) AND ADDRESS(ES)
OHIO STATE UNIVERSITY
1960 KENNY RD
COUMBUS, OH
US

8. PERFORMING ORGANIZATION REPORT NUMBER

9. SPONSORING/MONITORING AGENCY NAME(S) AND ADDRESS(ES)	10. SPONSOR/MONITOR'S ACRONYM(S)	11. SPONSOR/MONITOR'S REPORT NUMBER(S)
Air Force Office of Scientific Research 875 N. Randolph St. Room 3112 Arlington, VA 22203	AFRL/AFOSR RTB1	AFRL-AFOSR-VA-TR-2024-0065

12. DISTRIBUTION/AVAILABILITY STATEMENT
A Distribution Unlimited: PB Public Release

13. SUPPLEMENTARY NOTES

14. ABSTRACT
Among the characterization techniques which allow to “see” single atoms, atom probe tomography (APT) is unique in the way that individual atoms, instead of a collection of atoms, can be imaged while at the same time, the collected data can provide threedimensional information of atomic structures via reconstruction. In APT, individual or molecular species are field-evaporated from a sharp needle shaped specimen under an intense electric field and fly towards a 2D detector where their impact is recorded. The collective impacts form a “field desorption pattern” revealing the crystallographic structure of the specimen. While the patterns reveal the crystallography and atomic arrangement, they are not free of artefacts, and it is nearly impossible to quantify the resulting uncertainty in reconstruction due to the fully destructive nature of the technique. The major accomplishment in this project was the successful development of a predictive, hi-fidelity fully physical forward modeling code, “TAPSim-MD”, for field evaporation. With this, we have explained artifacts in field desorption patterns such as high-density zone lines, artifacts in reconstruction from unexpected evaporation sequences, and the resolution limit of APT when it comes to placing atoms in the reconstruction, which can easily be ~2 nm, way larger than the atomic size. Along with TAPSim-MD, we have also developed a novel method to quantify bond energies from DFT calculations, which not only allows to understand surface binding and evaporation sequences, but as a side project allows thermodynamics of alloys and intermetallic on a simple intuitive, yet physically fully quantitative level. We finally have shown that our simulation data are suitable to train deepneural network-based reconstruction models that, when applied to experimental data, can indeed get APT down to atomic resolution and eliminate the worst artifacts.

15. SUBJECT TERMS

16. SECURITY CLASSIFICATION OF:			17. LIMITATION OF ABSTRACT	18. NUMBER OF PAGES
a. REPORT U	b. ABSTRACT U	c. THIS PAGE U	UU	66

19a. NAME OF RESPONSIBLE PERSON	19b. PHONE NUMBER *(Include area code)*
ALI SAYIR	426-7236

Standard Form 298 (Rev.5/2020)
Prescribed by ANSI Std. Z39.18

DISTRIBUTION A: Distribution approved for public release.

AFOSR Final Report

FA9550-19-1-0378: Quantification of Atom Probe Tomography Data

PI: Wolfgang Windl
The Ohio State University

Co-PI: Emmanuelle Marquis
University of Michigan

Among the characterization techniques which allow to "see" single atoms, atom probe tomography (APT) is unique in the way that individual atoms, instead of a collection of atoms, can be imaged while at the same time, the collected data can provide three-dimensional information of atomic structures via reconstruction. In APT, individual or molecular species are field-evaporated from a sharp needle shaped specimen under an intense electric field and fly towards a 2D detector where their impact is recorded. The collective impacts form a "field desorption pattern" revealing the crystallographic structure of the specimen. While the patterns reveal the crystallography and atomic arrangement, they are not free of artefacts, and it is nearly impossible to quantify the resulting uncertainty in reconstruction due to the fully destructive nature of the technique.

The major accomplishment in this project was the successful development of a predictive, hi-fidelity fully physical forward modeling code, "TAPSim-MD", for field evaporation. With this, we have explained artifacts in field desorption patterns such as high-density zone lines, artifacts in reconstruction from unexpected evaporation sequences, and the resolution limit of APT when it comes to placing atoms in the reconstruction, which can easily be ~2 nm, way larger than the atomic size. Along with TAPSim-MD, we have also developed a novel method to quantify bond energies from DFT calculations, which not only allows to understand surface binding and evaporation sequences, but as a side project allows thermodynamics of alloys and intermetallics on a simple intuitive, yet physically fully quantitative level. We finally have shown that our simulation data are suitable to train deep-neural network-based reconstruction models that, when applied to experimental data, can indeed get APT down to atomic resolution and eliminate the worst artifacts.

DISTRIBUTION A: Distribution approved for public release.

1. Articles

Within this project, FA9550-19-1-0378, the following articles were published:

1. J. Qi, C. Oberdorfer, E. A. Marquis, and W. Windl, *Origin of Enhanced Zone Lines in Field Desorption Maps*, Scripta Materialia **230**, 115406 (2023).
2. T. Li, S.-C. Chien, Z. Ren, W. Windl, F. Ernst, and G. S. Frankel, *Understanding the Efficacy of Concentrated Interstitial Carbon in Enhancing the Pitting Corrosion Resistance of Stainless Steel; response to Further Comment by Martin et al.*, Scripta Materialia **237**, 115647 (2023).
3. A. Hegde, E. Weiss, W. Windl, H. Najm, and C. Safta, *Bayesian calibration of interatomic potentials for binary alloys*, Computational Materials Science **214**, 11660 (2022).
4. E. J. Weiss, L. Ward, C. Oberdorfer, T. Withrow, D. C. Riegner, A. Agrawal, and W. Windl, *Rapid production of accurate embedded-atom method potentials for metal alloys*, arXiv preprint arXiv:2208.02223 (2022).
5. J. Qi, C. Oberdorfer, W. Windl, and E. A. Marquis, *Ab initio simulation of field evaporation*, Physical Review Materials **6**, 093602 (2022).
6. J. Qi, C. Oberdorfer, E. A. Marquis, and W. Windl, *Ab-Initio Simulation of Field Evaporation in Atom Probe Tomography: Enhanced Zone Lines and Mixed-Layer Reconstructed Structures*, Microsc. Microanal. **29** (S1), 607-608 (2023).
7. T. Li, S.-C. Chien, Z. Ren, W. Windl, F. Ernst, and G. S. Frankel, *Understanding the Efficacy of Concentrated Interstitial Carbon in Enhancing the Pitting Corrosion Resistance of Stainless Steel; response to Comment by Martin et al.*, Scripta Materialia **224**, 115084 (2023).
8. X. Guo, H.-L. Huang, M. Zhu, K. Hariharan, S.-C. Chien, N. Huynh, J. Hwang, W. Windl, C. D. Taylor, E. J. Schindelholz, G. S. Frankel, *Interstitial elements created via metal 3D printing*, Materials Today **66**, 92-104 (2023).
9. W. Windl and S.-C. Chien, *Free-Energy Parameterization and Thermodynamics in Si-Ge -Sn Alloys*, Phys. Status Solidi B **259** (7), 2100590 (2022).
10. Y Y. Wang, Z. Chen, W. Windl, and J.C. Zhao, *Nonlinear Arrhenius behavior of self-diffusion in β-Ti and Mo*, Phys. Rev. Mater. **6** (6), 063402 (2022).
11. J. Qi, C. Oberdorfer, E. A. Marquis, and W. Windl, *Origin of High-Density Zone Lines in Field Desorption Patterns of Tungsten*, Microsc. Microanal. **28** (S1), 714-716 (2022).
12. A. Hegde, E. Weiss, W. Windl, H. Najm, and C. Safta, *Bayesian calibration of interatomic potentials for binary alloys*, Sandia National Laboratories Report SAND2022-4476C (2022).
13. F. Xue and E. A. Marquis, Role of diffusion-induced grain boundary migration in the oxidation response of a Ni-30Cr alloy, Acta Materialia **240**, 118343(2022).
14. T. Li, S.-C. Chien, Z. Ren, W. Windl, F. Ernst, and G. S. Frankel, *Understanding the Efficacy of Concentrated Interstitial Carbon in Enhancing the Pitting Corrosion Resistance of Stainless Steel*, Acta Materialia **221**, 117433 (2021).
15. J. Qi, C. Oberdorfer, E. A. Marquis, and W. Windl, *Full "Ab-Initio" Simulation of*

DISTRIBUTION A: Distribution approved for public release.

Field Evaporation of Samples with Grain Boundaries, Microsc. Microanal. **26** (S2), 2878-2879 (2020).

16. I. Ghamarian, L.-J. Yu, and E. A. Marquis, *Quantification of solute topology in atom probe tomography data: application to the microstructure of a proton-irradiated Alloy 625*, Metall. Mater. Trans A **51**, 42-50 (2020).
17. I. Ghamarian and E. A. Marquis, *Hierarchical Density-Based Cluster Analysis Framework for Atom Probe Tomography Data*, Ultramicroscopy **200**, 28-38 (2019).
18. I. Ghamarian and E. A. Marquis, *Morphological classification of dense objects in atom probe tomography data*, Ultramicroscopy **215**, 112996 (2020).

Under review is the following paper:

19. A. Hegde, E. Weiss, W. Windl, H. Najm, and C. Safta, *Bayesian Calibration with Embedded Model Error for Model Diagnostics*, International Journal for Uncertainty Quantification, article ID IJUQ-51602.

In preparation are the following two papers:

20. J. Qi, F. Xue, C. Oberdorfer, E. A. Marquis, and W. Windl, *Revisiting the field evaporation sequence in TiAl* (preprint on ArXiv).
21. J. Qi, C. Oberdorfer, E. A. Marquis, and W. Windl, *Orientation Bias in APT Reconstruction: GP Zones in Al-Cu Alloys.*

2. Presentations

1. **J. Qi**, C. Oberdorfer, E.A. Marquis, and W. Windl, *Full-Dynamics Field Evaporation Simulation: Overcoming Limitations of Transition State Theory for Atom Probe Tomography*, oral presentation, Microscopy and Microanalysis, Minneapolis, MN, 7/23/2023.
2. **J. Qi**, C. Oberdorfer, E.A. Marquis, and W. Windl, *Full-Dynamics Field Evaporation Simulation: Overcoming Limitations of Transition State Theory for Atom Probe Tomography* (Invited), Max-Planck-Institut für Eisenforschung GmbH, online, 8/30/2023.
3. **J. Qi**, C. Oberdorfer, E.A. Marquis, and W. Windl, Full-Dynamics Field Evaporation Simulation: Overcoming Limitations of Transition State Theory for Atom Probe Tomography, oral presentation, Materials Research Society Fall Meeting, Boston, MA, 11/26/2023.
4. **W. Windl**, *Do Bond Energies Explain It All?* (Invited), Workshop on Possibilities and Limitations of Quantitative Materials Modeling and Characterization, Bernkastel-Kues, Germany, May 16, 2023.
5. **J. Qi**, C. Oberdorfer, E.A. Marquis, and W. Windl, Origin of High-Density Zone Lines in Field Desorption Patterns of Tungsten, poster presentation, Microscopy and Microanalysis, Portland, OR, 7/31/2022.
6. **W. Windl**, C. Oberdorfer, E.A. Marquis, and J. Qi, *Full Ab-Initio Simulation of Atom Probe Tomography* (Invited), Workshop on Possibilities and Limitations of Quantitative Materials Modeling and Characterization, Bernkastel-Kues, Germany, May 25, 2022.

DISTRIBUTION A: Distribution approved for public release.

7. **J. Qi**, C. Oberdorfer, E.A. Marquis, and W. Windl, Full "Ab-Initio" Simulation of Field Evaporation of High Entropy Alloys, poster presentation, TMS (virtual meeting), 3/15/2021.
8. **W. Windl**, C. Oberdorfer, E.A. Marquis, and J. Qi, *Full "Ab Initio" Simulation of Field Evaporation Processes* (Invited), Atom Probe Tomography & Microscopy 2021, Virtual, September 28, 2021.
9. **J. Qi**, C. Oberdorfer, E.A. Marquis, and W. Windl, Full "Ab-Initio" Simulation of Field Evaporation of High Entropy Alloys, poster presentation, Materials Science & Technology (virtual meeting), 11/2/2020.
10. **J. Qi**, C. Oberdorfer, E.A. Marquis, and W. Windl, Full "Ab-Initio" Simulation of Field Evaporation of Samples with Grain Boundaries, poster presentation, Microscopy and Microanalysis (virtual meeting), 8/3/2020.
11. **I. Ghamarian**, E. Marquis, "Morphological Classification of Dense Objects in Atom Probe TomographyData" (invited), TMS (Feb 2020), San Diego, USA.
12. **Y. He**, D. E. Perea, S. X. Mao, C. Wang, T. Withrow, C. Oberdorfer and W. Windl, "In-situ HR-TEM and Simulation of Si Field Emitter Tips under Field Evaporation", Microscopy & Microanalysis Meeting (2019), Portland, USA.
13. **C. Oberdorfer**, T. Withrow, E. Marquis and W. Windl, Atomistic Simulation Based Modeling of APT" (invited), Microscopy & Microanalysis Meeting (2019), Portland, USA.
14. **I. Ghamarian** and E. A. Marquis, "Development and Application of an Integrated Framework of Hierarchical Density-based Cluster Analysis for Challenging Atom Probe Tomography Datasets", TMS (Mar 2019), San Antonio, USA

3. People

1. Dr. Christian Oberdorfer (Postdoc and Humboldt Fellow, OSU, 2017- Dec. 2019)
2. Jiayuwen Qi (OSU, PhD student, 2019-2023; graduating December 2023)
3. Dr. Iman Ghamarian (Postdoc, UM)
4. Dr. Fei Xue (Postdoc, UM)

4. Awards

1. **Jiayuwen Qi**, 2023 Graduate School Presidential Fellowship, The Ohio State University.
2. **Jiayuwen Qi**, 2023 M&M Student Scholar Award, jointly from Microanalysis Society and Microscopy Society of America.
3. **Emmanuelle Marquis,** 2023, Brimacombe Medalist, The Minerals, Metals & Materials Society: TMS.
4. **Wolfgang Windl**, 2022 Institute for Materials Science Distinguished Faculty Scholar Award, Los Alamos National Laboratory.
5. **Emmanuelle Marquis,** 2021, J.H. Block Lecture, International Field Emission Society

DISTRIBUTION A: Distribution approved for public release.

6. **Wolfgang Windl**, 2020 Faculty Diversity Excellence Award from the College of Engineering, OSU.
7. **Emmanuelle Marquis,** 2020 Fellow, International Field Emission Society.
8. **Emmanuelle Marquis,** 2020 Faculty Recognition Award, University of Michigan.
9. **Wolfgang Windl**, 2019 ASEE Best Paper in Graduate Studies Award.
10. **Wolfgang Windl**, 2019 ASEE Best Diversity Paper Award.
11. **Wolfgang Windl**, 2019 Lumley Interdisciplinary Research Award from the College of Engineering, OSU.
12. **Jiayuwen Qi,** 2019 University Distinguished Fellowship, The Ohio State University
13. **Christian Oberdorfer,** Awardee at the 14th Annual International Scholar Research Exposition, Office of International Affairs, OSU (11/7/2019, see picture).

Fig. 1. Award ceremony at the 14th Annual International Scholar Research Exposition, Office of International Affairs, OSU on 11/7/2019. Left to right: Associate Vice Provost Fernando Unzueta, Dr. Chris Oberdorfer, Dr. Wolfgang Windl, Dr. Szu-Chia Chien (all Windl Lab).

DISTRIBUTION A: Distribution approved for public release.

5 Technical Accomplishments

In modern material research and development, microscopy techniques with atomic-scale resolution have become indispensable to understanding material micro-structures and their relationship with material properties. On the road to atomic-scale resolution and indeed "seeing" atoms, a variety of microscopy techniques have been developed. Among them, electron microscopy related techniques dominate the 2D world of microscopy and microanalysis, as the wavelength of electrons is naturally suitable for imaging individual atoms. However, when we go from two to three dimensions, the capabilities of electron microscopy are still limited. Although the recently developed atomic electron tomography is able to create 3D atomic reconstructions, it can only deal with samples with very limited size and provide very limited chemical resolution up to now. Atom probe tomography (APT), on the other hand, was born as a dedicated 3D characterization technique decades ago. What makes APT unique is that there are no external imaging beams needed to resolve the structure such as light, electron, or ion beams. Atoms in the specimen are imaged by themselves via field evaporation, therefore, data collected in APT naturally involves 3D information about the specimen and can resolve both positions and chemical identities of individual atoms in bulk materials with an appropriate reconstruction method.

The practice of Atom Probe Tomography (APT) dates back to the 1970s. During its early years, various names were employed to describe specific instruments and atom probe methods. However, as time has passed and this 3D characterization technique has evolved, the widely accepted and generic term "atom probe tomography" has emerged within the community to collectively refer to this method [1].

APT starts with field emission of atoms of the emitter itself by application of a large electric field and serves as the fundamental physical process of APT. By adding recording devices to record impact sequence and positions of evaporated atoms, the 3D coordinates of the collected atoms can be determined. After decades of development, APT eventually evolved into the design currently in use, known as local electrode atom probe (LEAP) [2].

"Tomo" in tomography comes from the Greek word *tomos* meaning "section" or "slice", while the origin of the word atom is *atomos*, meaning "indivisible". Indicated by tomography, where *graphia* means recording, the term atom probe tomography is used to refer to the atom probe technique recording data from evaporating slice by slice, or surface layer after surface layer, which then are reassembled to produce three-dimensional images of a specimen.

5.1 Basic setup in APT experiments

In APT, atoms in the specimen are imaged by themselves via field evaporation, therefore, data collected in APT naturally involves 3D information about the specimen. To realize field evaporation, the geometry of APT is very uniquely designed in order to create very high electric fields on demand, which are on the order of 10 V/nm. To generate a 10 V/nm uniform field within 1 cm, a 10^5 kV voltage needs to be applied. Besides

DISTRIBUTION A: Distribution approved for public release.

the extremely high voltage, this field is high enough to induce field emission of electrons from the cathode which could cause breakdown even if ideal vacuum conditions had been reached. In order to create a manageable experimental setup in light of these challenges, a needle-shape specimen is prepared, which is also called a field emitter in the context of field evaporation, where the large curvature of the surface around the apex locally creates an electric field of the needed magnitude. A specimen needs to be sharpened to less than 100 nm in tip diameter to create a field high enough for evaporation around the apex with a moderately high applied voltage (about 10 kV), which in current state-of-the-art is achieved by the focused ion beam (FIB) technique.

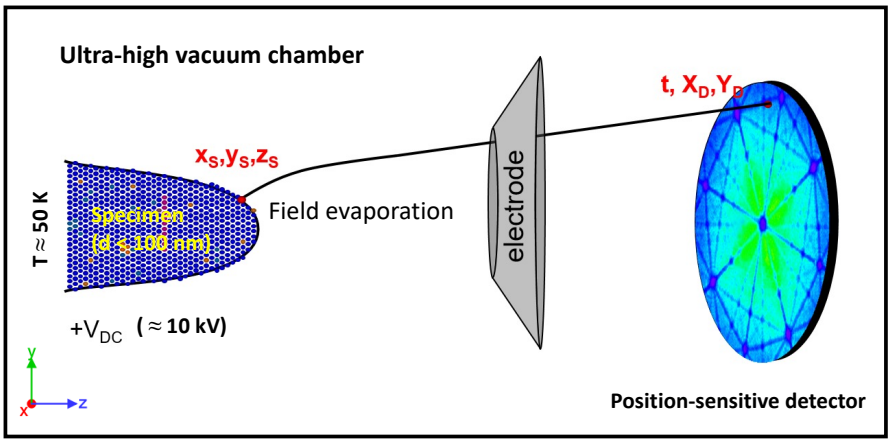

Figure 1: Schematic diagram of an atom probe microscope.

A schematic diagram of APT is shown in Fig. 1. APT experiments are conducted at very low temperatures (about 50 K) in an ultra-high vacuum chamber. In the state-of-the-art LEAP instrument, the specimen is attached to a positive electrode, while a counter electrode with a central circular aperture is set close to the specimen, which is called a local electrode as appearing in the name LEAP. To control field evaporation of single atoms, the specimen is held at a positive standing voltage V_{st} relative to ground, then atoms are field evaporated by either applying a negative high-voltage pulse V_{pulse} relative to ground to the counter electrode, which is called voltage pulse mode; or applying a focused UV laser pulse to the specimen surface, which is called laser pulse mode [1].

Once atoms leave the specimen surface, they will keep traveling until they hit a single-ion detector consisting of a pair of microchannel plates and a crossed delay line position sensitive sensor, which records the impact coordinates and sequence of arriving ions. Time-of-flight mass spectrometry is used to reveal the chemical information of detected ions. The flight times are measured with a time-to-digital converter, starting with the pulse signal and ending with ions hitting the detector [1].

DISTRIBUTION A: Distribution approved for public release.

5.2 APT data

Collected data in an APT experiment compose the field evaporation map on the detector, where the impacting evaporated particles are recorded with timestamp and mass-analyzed. The time sequence of these 2D data can then be used for 3D reconstruction, as described in the following two sections.

5.2.1 2D Data: Field Evaporation Maps

In the context of APT, a 2D image depicting the cumulative impacts of the collected ions on the detector is called a field evaporation map. The intensity of impacts is often indicated by different colors or a bright contrast shown on detectors in early instruments. Field evaporation maps often display distinctive features such as concentric ring patterns around poles depleted in hit intensity, as well as depleted and sometimes enhanced zone lines connecting poles. The poles are indexed based on stereographic projections of normals to the corresponding crystal facets of the specimen crystal structure in the orientation of measurement. Although atom trajectories in field evaporation are not governed by any simple projection relationship, such projections are still used for the purpose of indexing because they preserve angular relationships between facets [1]. The depleted center of poles is traditionally rationalized via local magnification, space-charge repulsion of atoms evaporating simultaneously, and surface diffusion. The concentric rings have been associated with the curvature of the sample and been attributed to periodic variations in the "aiming errors" (another way to talk about lateral velocity variations) caused by the concentration of local fields on the edges.

Dark and bright zone lines are structure- and material-dependent and are related to the faceting of the surface. While the formation of dark zone lines has also been explained by the "aiming errors" and could be reproduced in previous simulations without desorption dynamics [3], the literature did not provide any conclusive, data-driven explanation about the enhanced zone lines, except for some undemonstrated hypotheses. It was one of the seminal successes of the present work to identify their origin based on a new simulation approach. We found that the misalignment of the electrostatic forces and interatomic forces deviates the launch direction of certain atoms away from the local electric field direction, giving rise to an accumulation of hit events around zone lines. The exact mechanism will be discussed in detail in Sec. 5.7.

5.2.2 3D Data: Standard Reconstruction Approach

The 3D imaging capability of APT is enabled by reconstruction, and it determines the quality of the 3D information obtained for further analysis about local composition and structure. Reconstruction converts the 2D coordinates collected by the detector and time information into 3D coordinates representing atom positions, which in the end results in a distribution or cloud of atoms in 3D.

The reconstruction protocol was first proposed by Bas et al. in 1995 [4] and is still in use in more or less unchanged fashion. In this protocol, there are two main assumptions regarding atom trajectories and the emitter shape: first, atoms are evaporated layer by

DISTRIBUTION A: Distribution approved for public release.

layer from the edge of an atomic terrace, and atom trajectories follow a straight-line projection law; second, the emitter tip always remains spherical but recedes linearly with time, providing z-coordinate information. These two assumptions then result in a simple conversion algorithm between the 2D and 3D coordinates.

The in-plane coordinate (x, y) orthogonal to the specimen axis can be reconstructed from the 2D coordinate $(X_{\mathrm{det}}, Y_{\mathrm{det}})$ on the detector by performing linear back projection:

$$x = X_{\mathrm{det}} \cdot (r/\xi)/L \tag{1}$$
$$y = Y_{\mathrm{det}} \cdot (r/\xi)/L, \tag{2}$$

where r is the curvature radius of the tip, and L is the distance between the specimen and detector. The exact distance in the equations should be different from L, but since $L \gg r$, this distance approximates to L. ξ is an image compression factor, which describes the lens-like effect of the electric field that bends atom trajectories from their launch directions towards the specimen axis. ξ is defined as the ratio of θ' to θ, where θ' is the imaging angle, $\theta' = \sqrt{X_{\mathrm{det}}^2 + Y_{\mathrm{det}}^2}/L$; θ is the actual launch angle of an evaporated atom, which is usually assumed to be perpendicular to the local surface. Due to the bending effect of the electric field, θ' is always smaller than θ, therefore, $\xi < 1$. ξ should be somewhere between a stereographic projection ($\xi = 0.5$) and a radial projection ($\xi = 1$), and it can be determined by comparing these two angles for certain indexed poles.

In order to determine the z-coordinate of the detected atoms, one starts by flipping the evolution direction of the tip, i.e., the apex of the tip moves along the positive direction of the z-axis. Assuming the apex of the spherical tip is $(0, 0, z_{\mathrm{apex}})$, the z-coordinate of the recorded atom should be

$$\begin{aligned} z &= z_{\mathrm{apex}} + r \cdot (1 - cos\theta) \\ &= z_{\mathrm{apex}} + r \cdot \left[1 - cos(\theta'/\xi)\right]. \end{aligned} \tag{3}$$

Next, we need to model how the apex position changes as the experiment progresses. Since field evaporation of atoms in APT occurs layer by layer, the emitter shrinks during the experiment, and the apex position of the emitter has to be updated accordingly. Assuming a linear dependence, the z coordinate of the apex after evaporation of $i + 1$ atoms becomes

$$z_{\mathrm{apex}}^{(i+1)} = z_{\mathrm{apex}}^{(i)} + dz, \tag{4}$$

where dz is an average increment of the apex position per detected atom. Postulating the conservation of volume leads to

$$N \cdot dz \cdot \pi(r \cdot sin\theta_D)^2 = \Omega \cdot N/p_{\mathrm{det}} \tag{5}$$
$$dz = \Omega/(\pi r^2 \cdot sin^2\theta_D \cdot p_{\mathrm{det}}), \tag{6}$$

where N is the number of atoms detected, θ_D is the angular field-of-view, Ω is the average atomic volume, p_{det} is the detection efficiency which is added to account for undetected atoms.

DISTRIBUTION A: Distribution approved for public release.

5.3 Quantitative APT Analysis – Uncertainties and Challenges

APT possesses a distinctive capability of simultaneously resolving the chemical identities and 3D positions of atoms. Consequently, it is exceptionally well-suited for characterizing heterogeneous microstructures, including features like grain boundaries, precipitates, clusters, and the distribution of solutes in alloys. Despite the assertion that APT offers "atomistic" resolution since it directly detects atoms, the APT community faces a substantial challenge in realizing its full quantitative potential. Several factors contribute to the difficulties in elevating APT to a truly quantitative imaging and analysis technique.

First, field evaporation is a destructive process, therefore, there is no way to confirm the original positions of the detected evaporated atoms via experiment. In order to identify where the evaporated atoms come from, various forward modeling tools have been developed where trajectories of each single atom are traceable. However by the beginning of this work, there were no modeling tools able to entirely address the complexity of field evaporation. The existing atomistic modeling methods of field evaporation in APT will be discussed in detail in Sec. 5.3. Thus, while forward modeling offers unique chances in understanding uncertainties and improve reconstruction algorithms, the lack of high-fidelity models has been an obstacle for the full understanding of the complex physics involved in field evaporation and consequently has been limiting the interpretation of artifacts in APT data.

Second, the standard reconstruction approach used to process the data relies on highly simplified assumptions as discussed in Sec. 5.2.2. These assumptions are rarely fulfilled, especially for materials with multi-components and complex structures, which further introduce artifacts. Figure 2 is an example of reconstruction failure in a complex multi-layer sample compared to the TEM image of the tip's shape [5]. Due to the assumptions about ideal evaporation sequences and spherical shape of the emitter in the standard reconstruction approach, the reconstruction produces a bowl-shape FeCo layer above the MgO, which bears very little resemblance in all respects to the actual sample. Artifacts in reconstruction usually come from a combination of three sources: (1) a non-spherical tip shape; (2) a non-ideal evaporation sequences usually caused by different evaporation fields due to different bonding situations of the different components, where an atom with a higher evaporation field tends to stay on the surface, while an atom with a lower one tends to leave early; and (3) aberrations of atom trajectories from ideal paths following the projection law, which may be caused by surface migration, surface reconstruction, aberrations of local electric fields, and aberrations of initial velocities due to interatomic interactions competing with the external electrostatic forces. Improvements on the standard approach has been mainly focused on a better estimation of the reconstruction parameters, e.g., the image compression factor or the global and local curvature of the emitter tip [6, 7, 8, 9]. Other "tricks" are also employed in the current commercial software in an attempt to accommodate data to appropriate values, e.g., by introducing the constraint of a uniform reconstructed density of atoms, or calibration of lattice spacings to theoretical values [10]. Despite all these improvements, the 30-year old framework of APT reconstruction is still unchanged. Revolutionary approaches have to be proposed to cope with all the artifacts and fundamentally improve

DISTRIBUTION A: Distribution approved for public release.

the reconstruction, and they have no choice but to closely rely on the development of modeling approaches.

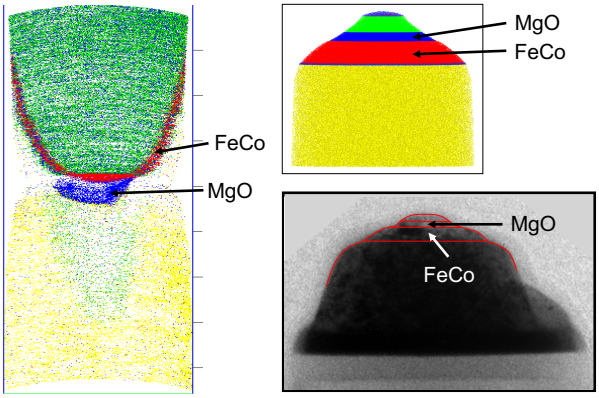

Figure 2: Reconstruction failure in a complex multilayer sample: (a) is the standard reconstruction of experimental data; (b) is the virtual tip shape in simulation which gives a similar tip shape compared to the real tip shown in (c); and (c) is the transmission electron microscopy image of a specimen partially field evaporated up to MgO layer. Figures courtesy Prof. Emmanuelle Marquis after Ref. [5].

Finally, the quantification of microstructures from the raw or reconstructed APT data has remained limited to basic analysis without considering any statistical variations or errors. A more holistic approach to data processing is needed to assign positional uncertainties to the Dirac function based data, i.e., besides mapping atoms to certain reconstructed (x, y, z) coordinates, some uncertainties of each reconstructed position need to be determined, resulting in an "origin-likelihood" distribution for each atom. Such approaches have been maturing over the past decade in many areas of physical research and are by now well enough understood. As a pertinent example, the state-of-the-art interatomic potential development process involves by now Bayesian uncertainty quantification with embedded error quantification for the modeled quantities of interest such as energies, forces, or structural and elastic parameters [11, 12]. Such an uncertainty quantification will need to include both APT simulation and experiment and an optimization process that merges experimental observations and simulation results.

As discussed in Sec. 5.2.2, it is impossible to validate reconstructed coordinates of evaporated atoms experimentally as specimens have been destroyed after APT experiments. In this case, forward modeling and simulation play an essential role in interpreting APT data, understanding the fundamental processes in APT, and further improving the reconstruction process and the quantitative capability of the APT technique.

Several forward modeling approaches have emerged alongside the development of the APT technique, ranging from the continuum to atomistic scales [13]. In its early stages, simulations were employed to elucidate the evaporation sequence and the evolution of surface morphology [14, 15]. These models were primarily based on emitter geometry

DISTRIBUTION A: Distribution approved for public release.

and did not account for field effects.

Subsequently, continuum models were developed, primarily focusing on simulating the dynamic changes in the emitter shape during field evaporation to study deviations from the ideal hemispherical assumption. The data generated from these simulations have proven valuable in guiding reconstruction efforts, particularly in improving reconstruction parameters such as the local curvature of the emitter tip surface [16, 17, 18, 19, 20, 9]. These approaches are computationally efficient and capable of modeling real-size emitter geometries while tracking shape evolution.

However, these continuum models lack real atomic structures, making them unsuitable for studying atom behavior during field evaporation or simulating crystallographic features related to specimen crystal structures. Consequently, they are limited to generating artificial atom trajectories and field evaporation patterns.

On the opposite end of the spectrum, first-principles investigations of field evaporation have ventured into exploring the electronic aspects of this phenomenon over the past 20 years. For instance, density functional theory (DFT) has been applied to examine the bond-breaking processes associated with field evaporation pathways proposed within different evaporation mechanisms [21]. Several studies have also targeted the calculation of field evaporation energies by DFT in the presence of an electric field or by using the Müller formula based on binding energy, work function, and ionization energy [22] to find zero-barrier evaporation fields, i.e. the field value where the evaporation barrier goes to zero, either for isolated adatoms on a flat surface or as a function of varying surface morphology [23, 24, 25, 26, 22, 27, 28, 29].

While first-principles approaches are known for their accuracy, applying them to APT simulations presents a formidable challenge due to the immense computational resources required. As a result, these efforts have been limited to systems containing only a few hundred atoms with simplified, slab-like structures and very brief time scales. This limitation has been preventing a comprehensive first-principles examination of the complete field evaporation process for realistic specimens subjected to realistic electric fields. Nonetheless, the prospect of more complete first-principles approaches in the not too distant future is there, considering the continuously increasing emergence of fast electronic structure methods [30, 31, 32] and the availability of increasingly powerful computational resources on the exascale [33].

Considering the need of investigating crystallographic features and atom behavior in field evaporation, and at the same time, the limits of the currently accessible computational power, atomistic modeling is the currently most promising compromise between DFT-level accuracy and continuum efficiency, which is what we have developed within this project.

5.4 Transition state theory and previous modeling approaches

5.4.1 Thermal Activation Based Escape Models

As mentioned previously, field evaporation is a phenomenon where surface atoms of a specimen are ionized and emitted by a very large applied electric field. Field evaporation

DISTRIBUTION A: Distribution approved for public release.

is a rather complex process including bond breaking and ionization of atoms which further involves complex, time-dependent electronic processes in the presence of a very large electric field. The exact mechanism of field evaporation is still under debate, where the most controversial part concerns when and where the ionization process happens. Müller proposed a seminal model to describe this process [34], which is now known as the image hump model. Potential energy curves in the image hump model are shown in Fig. 3. Within this model, it is assumed that full ionization occurs first, and the charged ion then has to conquer an energy barrier created by the Schottky effect to escape to vacuum [35]. In contrast, Gomer later proposed charge-exchange-type models

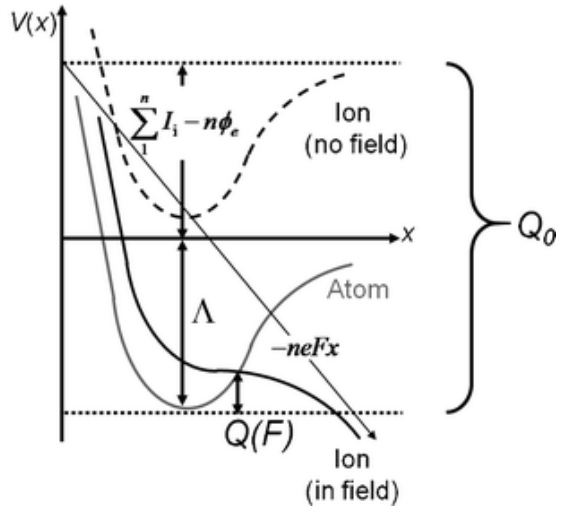

Figure 3: Atomic and ionic potential energy diagram with and without electric field assumed within the image hump model. V is the potential energy, Λ is the sublimation energy, n is the degree of ionization, I_i is the i^{th} ionization energy, ϕ_e is the work function, Q_0 and $Q(F)$ are energy barriers without and with electric field F respectively. This figure is reproduced from Ref. [36].

[37] where it is assumed that ionization and escape occur simultaneously around the top of the energy barrier [35]. In spite of the debate, it is generally believed that field evaporation is a thermally activated process. Based on the thermal activation theory, the evaporation-rate constant (k_n) for escape of atoms with charge n can be written as an Arrhenius type equation,

$$k_n(F,T) = A_n exp[-Q_n^{\mathrm{EV}}(F)/(k_B T)], \tag{7}$$

where A_n is the escape-attempt frequency, $Q_n^{\mathrm{EV}}(F)$ is the field evaporation (EV) activation energy for an atom escaping as a $+n$-charged ion under the local field F, k_B is the Boltzmann constant, and T is the temperature. The energy along the local field direction, considering only the field dependence of the formed ions and ignoring any quantum mechanical effects, can be expressed as

$$Q_n(F,x_n) \approx K_n^0 - neFx_n - n^2e^2/16\pi\varepsilon_0 x_n, \tag{8}$$

where x_n is the distance from the surface, and K_n^0 is the thermodynamic term which is defined by

$$K_n^0 \equiv \Lambda^0 + H_n - n\phi. \tag{9}$$

DISTRIBUTION A: Distribution approved for public release.

Λ^0 is the zero-field sublimation energy, H_n is the total ionization energy of the first n charge states, and ϕ is the local work function. By setting the partial derivative of Q_n with respect to x_n to zero, the position of the energy barrier is found at

$$x_n^{\mathrm{EV}}(F) = \sqrt{ne/16\pi\varepsilon_0 F}. \tag{10}$$

The height of the energy barrier is therefore

$$Q_n^{\mathrm{EV}}(F) = K_n^0 - \sqrt{(n^3e^3/4\pi\varepsilon_0)\cdot F}. \tag{11}$$

By setting $Q_n^{\mathrm{EV}}(F)$ to zero, the zero-barrier evaporation field (ZBEF) can be calculated, which is the critical electric field required to eliminate the energy barrier of field evaporation [22]. Denominating the critical escape field calculated from Eq. 11 as Müller's formula,

$$F_n^M = (4\pi\varepsilon_0/n^3e^3)(K_n^0)^2, \tag{12}$$

the corresponding critical distance from the surface is the Müller escape distance,

$$x_n^M = 2n^2e^2/16\pi\varepsilon_0 K_n^0. \tag{13}$$

Although Müller's formula has a very simplified form, its estimation of ZBEF for different elements has an overall good agreement with the onset fields found in experiments [38]. This formula is still used today in estimating evaporation fields [22] and applied to reconstruction and simulations.

5.4.2 Previous Atomistic Modeling for APT

The first atomic level modeling of field emitters was proposed by Vurpillot et al. in 1999 [39], where the atomic structure of an elemental emitter was modeled by a 3D rigid cubic grid, and the surrounding electrostatic potential was determined within classical electrostatics from Laplace's equation ($\nabla^2 V = 0$). Later, a number of atomistic simulation approaches have been developed, and they all follow the general procedure based on Vurpillot's approach: (1) removal of the surface atom with the highest evaporation probability; (2) recalculation of the electric field distribution for the updated geometry; and (3) calculation of the trajectory of the evaporated atom by integration of Newton's equation of motion. Building on this approach, Geiser et al. introduced grids with different sizes, making the model compatible with any cubic structure emitter [40]. Oberdorfer et al. replaced the rigid lattice structure with adaptive unstructured meshes based on Voronoi cells, where the mesh at the tip is determined by the atom positions with increasing coarseness away from the tip [41]. Beyond Vurpillot's approach whose use of Laplace's equation restricted modeling to materials with infinite permittivity ε, Oberdorfer solved Poisson's equation ($\nabla^2 V = -\rho/\varepsilon$) to compute the electrostatic potential and electric field. This model is able to be applied to any structure with any surface morphology [42].

In such approaches, calculation of the evaporation probability of an atom is built on the thermal activation mechanism described in Sec. 5.4.1, where the evaporation rate is

DISTRIBUTION A: Distribution approved for public release.

taken to evaluate evaporation probability on each atom site, which is dependent on the evaporation activation energy of an atom under its local electric field as shown in Eq. 7. Neglecting any randomness caused by atomic motion at a finite temperature, the atom with the highest evaporation rate or probability should have the lowest energy barrier. Inserting Eq. 12 into Eq. 11, the energy barrier can be written as a function of the ratio between the local field F and the calculated ZBEF F_n^M from Müller's formula,

$$Q_n^{EV} = K_n^0(1 - \sqrt{F/F_n^M}). \tag{14}$$

When F is near F_n^M, the first order Taylor expansion gives a linear relationship between the energy barrier and the local field under the assumption of a constant F_n^M,

$$Q_n^{EV}(F) \approx K_n^0/2(1 - F/F_n^M). \tag{15}$$

From here, it is easy to compare the evaporation probabilities for atoms at different sites by comparing the ratios between local fields F and ZBEFs. Assuming a constant ZBEF for a single species of atoms, the atom exposed to the highest local electric field has the lowest energy barrier, therefore it possesses the highest evaporation probability. For atoms of different species exposed to electric fields of the same magnitude, the atom with the lowest ZBEF has the lowest energy barrier for a given F, therefore it possesses the highest evaporation probability in this case.

Several variations to this general approach have been examined. These include solving the electrostatic field from the Robin equation [43], which however has not been widely applied. A kinetic Monte Carlo (KMC) approach to add randomness to the choice of the evaporation event found little effect at experimental temperatures [44]. More impactful was the coupling of molecular dynamics (MD) with the finite element method in different simulation approaches [45, 46, 47, 48]. There, instead of a "static" tip structure, a "dynamic" tip structure is thermally equilibrated for several picoseconds after an atom is removed from the tip. Through the addition of surface dynamics, several artifacts could be reproduced and explained, for example, athermal surface migration of solute atoms with much stronger bonds [47], and redistribution of the electrostatic field following the field evaporation of atoms [49].

5.4.3 Challenges in APT Simulation From Transition State Theory

Evaporation processes within field ion emission happen on a rather long time scale compared to the thermal oscillations of the surface atoms (on the order of picoseconds), which classifies the evaporation events as infrequent events within the world of atomistic simulations. Previous field evaporation models as described in Sec. 5.4.1 are implicitly based on the harmonic transition state theory (TST) for infrequent events [50], where thermal activation is assumed to happen at a certain average rate τ depending on the temperature through the attempt frequency τ_0 and the activation energy Q. A harmonic approximation of the energy curve results in an Arrhenius equation $\tau = \tau_0 \exp(-Q/k_B T)$. The utility of TST in treating infrequent events such as atomic evaporation is based on two fundamental assumptions: first, that one knows in advance how an evaporation event

DISTRIBUTION A: Distribution approved for public release.

happens, i.e., a known escape path; and second, that one can find the relevant saddle points on the energy surface for these specific evaporation events to obtain corresponding activation energies. Therefore, TST can only predict the rate of transition from one state to another, but it is intrinsically incapable of predicting any dynamics between the two states.

With regard to modeling of field evaporation, although the current state of the art of TST-based methods has increased realism by adding atomic structure, realistic field, and atomic motion, one of the most crucial approximations, i.e. the convenient but unphysical separation of dynamics from the process of evaporation, has yet to be addressed. Consequently, these models have to assign an ad-hoc launch velocity to an evaporating atom, typically zero. However, such a choice biases calculation of atom trajectories and the resulting field evaporation map in a way that many distinct features in evaporation maps and reconstruction associated with full dynamics cannot be reproduced and explained [51]. This issue will be further discussed in Sec. 5.7. Moreover, activation energies in such approaches are usually estimated by using the simplified Eq. 15, where species-specific empirical evaporation fields or tabulated ZBEFs are often adopted in calculations. However, it has been shown in the previous DFT work that the activation energy depends rather sensitively on the specific configuration around the evaporating atom [22]. Last but not least, TST also assumes that there are no correlated events in the escape process, which on the contrary, is very likely to happen in field evaporation.

The shortcomings of TST to describe infrequent events are well known since a long time, as TST is a convenient approximation that was made a hundred years ago before the advent of computers fast enough to deal with full dynamics. As an alternative, MD methods with appropriate acceleration algorithms as needed have been in use for more than 25 years [52]. In this project, an MD based simulation approach has been developed to describe the infrequent event system in field evaporation and for the first time brings full dynamics to simulation of the field evaporation process.

5.5 Full-dynamics APT simulation tool – TAPSim-MD

5.5.1 Methodology

To enable full dynamics in simulation of field evaporation, we developed an MD based simulation tool – "TAPSim-MD" [53]. It combines the finite element Poisson equation solver from the APT simulation package TAPSim [41, 54] with the popular molecular dynamics simulation package LAMMPS (Large-scale Atomic/Molecular Massively Parallel Simulator) [55, 56]. Field evaporation is integrated as part of an MD simulation, where atoms move under the net forces composed of the usual interatomic forces and the electric-field induced electrostatic forces. Although the interaction between ions and neutral atoms should be considered explicitly, we find that the approximation of using standard interatomic potentials is good enough to capture the main characteristics and general trend of the field evaporation process. We demonstrate this by comparing TAPSim-MD results to those of density functional theory calculations in an example of elemental Al in Sec. 5.5.3. Our approach allows for the first time to describe the underly-

DISTRIBUTION A: Distribution approved for public release.

ing dynamics in the evaporation process, which is intrinsically impossible in TST-based approaches, and also eliminates the need for ad-hoc assumptions regarding the activation energy or the launch velocity. We will demonstrate in Secs. 5.7 - 5.9 that this approach is more realistic and can provide new understanding of composition dependence of evaporation field, local-environment effects, detailed evaporation mechanisms, their effects on the observed detector images, and artifacts in reconstruction.

The electrostatic force calculation follows Oberdorfer's method [41]. A key characteristic of this method is the meshing between Voronoi cells in the vacuum surrounding the tip and the atomic tip structure, where each atom is a node and chosen as the center of a Voronoi cell, and extra nodes are randomly distributed in the vacuum. The mesh becomes coarser away from the tip into the vacuum for computational efficiency. Inaccuracies from meshing can be minimized due to the adaptive distribution of Voronoi cells in addition to the emitter cells. After the mesh is established, the electrostatic potential can be solved from Poisson's equation on the mesh following the approach described in Ref. [42]. The electric field is calculated from the electrostatic potential through the numerical differentiation scheme for the irregular grid using the method based on interpolation between the generator points outlined in Ref. [41]. The polarization charge on each atom is then calculated from Gauss's law (even below the surface in case the material is not a metal and has a finite dielectric constant). The electrostatic force on each atom is obtained as a sum of forces induced on each facet of the atom cell from the product of the charge and the electric field. The force induced on atom i is written as

$$\vec{F_i} = -\sum_j \left(\frac{\varphi_j - \varphi_i}{|\vec{p_j} - \vec{p_i}|} \right)^2 \cdot 2 \cdot \varepsilon_0 \cdot \frac{\varepsilon_{r,j} - \varepsilon_{r,i}}{\varepsilon_{r,j} + \varepsilon_{r,i}} \cdot \frac{\vec{p_j} - \vec{p_i}}{|\vec{p_j} - \vec{p_i}|} \cdot ||A_{ij}||, \tag{16}$$

where $\{j\}$ are indices of neighbor cells, φ is the solved electrostatic potential for the node, $\vec{p}$ is the coordinate of the node, ε is the permittivity or dielectric constant of the cell, and $||A_{ij}||$ is the area of the facet between the two cells. For metals, the dielectric constant is infinite, which we approximate by a large but finite value of 10^6 to keep the numerics stable. Care needs to be taken for materials with strongly field-dependent dielectric constant such as $SrTiO_3$, where the dielectric constant in the range of evaporation fields is more than one order of magnitude smaller than in the field-free case [57].

Oberdorfer's method uniquely determines realistic electrostatic force contributions, which when added to the interatomic forces deduced from the applied interatomic potential, allows a full-dynamics simulation of field evaporation. The evaporation process happens naturally during an MD simulation, where an atom is pulled off the surface by the electrostatic force. This process can be detected through vanishing of the interatomic force or by defining a critical velocity for an atom. The sound velocity of the studied material is a convenient value. Calculation of trajectories after evaporation and recording of the data then follow again the procedure outlined in Ref. [41] by integrating equations of motion of evaporated atoms. While this approach may sound straightforward, marrying two major codes, especially from the two fundamentally different domains of finite-element modeling and atomic simulation required a large number of handshake steps and streamlining, especially since computational performance is essential to allow

DISTRIBUTION A: Distribution approved for public release.

for tips that are at least close to realistic dimensions in size and took several years.

In our MD simulations, we use a Langevin thermostat to keep the temperature of the emitter low targeting at 50 K, but this thermostat only works on atoms in the bulk, i.e., excluding the surface atoms, with a damping parameter of 2.50 and the total random force set to zero. The velocity-Verlet time integration algorithm is implemented via the NVE ensemble tag in LAMMPS for all atoms in the bulk and on the surface, although the system does not conserve energy. We employ this specific thermodynamic setting rather than directly applying the NVT ensemble for all atoms in the system in order to ensure that atoms on the surface can be correctly accelerated to evaporate. The default timestep is 1 fs for metal units used in LAMMPS. We first run 10,000 MD steps to compute equilibrium of the system without any electric field for initialization, then increase the voltage by a certain step as set in the input script, followed by running MD until one atom is determined detached within 1,000 MD steps or ending after 1,000 MD steps if no evaporation happens. The voltage will then be changed according to the setting, and the system will be updated in terms of the electric field, the number of atoms, the neighbor lists, the atom groups, etc. A new set of MD runs will then begin and end when one atom is determined detached within 1,000 MD steps or after 1,000 MD steps if no evaporation happens. In order to fix the position of the tip base to prevent drifting, we set for atoms in the bottom layer of the virtual tip all velocity components to zero, as well as the z-component of their forces. In addition, the "fix recenter" command is used to constrain the center-of-mass position of the bottom layer in the xy-plane.

Regarding the choice of interatomic potentials, we use embedded atom model (EAM) potentials in most of our simulations to balance accuracy and speed of computation, since the simulations are computationally rather intensive. EAM potentials are known to work very well for close-packed structures and can also work for bcc when the cutoff is long enough. When choosing a potential, we first pick a series of viable candidate potentials based on if their fitting database includes quantities relevant to field evaporation and run test simulations. The final decision about which potential to choose is based on the assessment of the test simulation results which should be stable and reasonable. We will discuss more about the effect of interatomic potentials on simulation results in Sec. 5.5.4.

5.5.2 Electrostatic Potential and Electric Field

The electrostatic potential and electric field distributions are examined in a W tip with a 10 nm radius and a height of 27 nm. Figure 4 (a) and (b) shows the calculated electric field and electrostatic potential for this tip. The potential drops rapidly from the tip surface to the vacuum space by about 75% within 44 nm along the central axis, which results in a strong electric field around the tip. The strongest field shown by the warmest color is around the top surface of the tip, which is about twice as large as the field around the side surface of the shaft.

Migunov et al. experimentally determined the electric field and electrostatic potential around a charged tip from a numerical analysis of charge density measurement on the tip surface from electron holography [58]. The distribution of the electrostatic potential and

DISTRIBUTION A: Distribution approved for public release.

electric field around the atom probe needle from this work is reprinted in Fig. 4c. The apex radius of the tip used in the experiment was about 15.6 nm, which is comparable to the virtual tip used in our simulation. The experimental result shows that the potential drops from the tip surface to the vacuum space by about 75% within 25 nm along the central axis, and the strongest field is found around the top surface of the tip and is about 4 times as large as the field around the side surface of the shaft. Considering the considerable uncertainties in charge density measurement paired with the strong approximations underlying the numerical analysis including the perfect cylindrical symmetry of the sample and the ellipsoidal shape of the tip, the agreement between our simulation and the experiment is good.

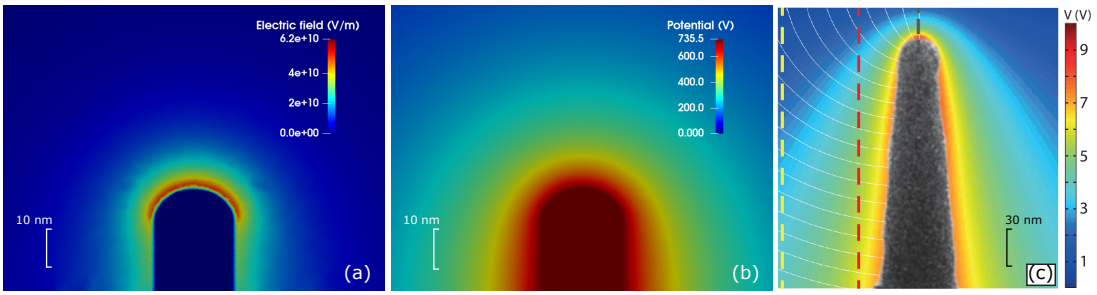

Figure 4: Contour plots of the (a) electric field distribution and (b) electrostatic potential distribution for the center of a 10 nm-radius virtual W tip. The potential in (b) between two nodes of the mesh is calculated by linear interpolation. The electric field in (a) is computed from the gradient of the potential. (c) is the distribution of the electrostatic potential and electric field around an atom probe needle from electron holography measurements. The white lines represent electric field lines. The colors correspond to equipotential contours. Figure (c) is reprinted from Ref. [58].

5.5.3 Force Comparison with DFT Results

The direction of the local electrostatic force calculated within the TAPSim-MD approach depends on the local surface morphology of the evaporating atom as it should. In the example shown in Fig. 5, the evaporating atom is protruding, and the direction of its electrostatic force is approximately normal to the envelope of the local surface, pointing outwards.

To examine if the superposition of induced electrostatic and interatomic forces is a reasonable approximation of the resulting total force, we conducted TAPSim-MD simulation for elemental Al and compared the results with published density functional theory (DFT) calculations for the evaporation of an Al adatom from a {111} Al substrate [23, 28].

In Fig. 6 (a) and (b), we determined the force vs. z-position from the energy E vs. z-position plots in Ref. [23] and [28] by numerically calculating the derivatives $-dE/dz$ at each position. The equilibrium positions for different field values were set to zero. A

DISTRIBUTION A: Distribution approved for public release.

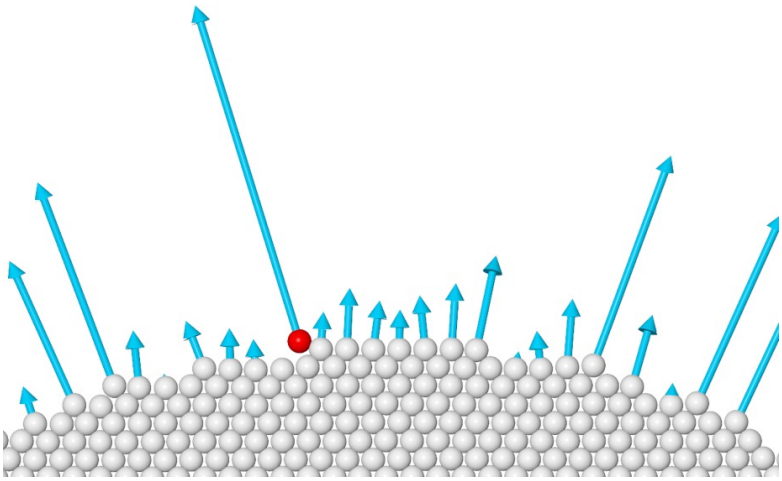

Figure 5: Side-view of a slab of a virtual 8 nm-radius ⟨011⟩ oriented W tip cut parallel to the z-axis. Blue arrows represent electrostatic forces with lengths proportional to their magnitudes. The red atom experiences the largest force and is evaporating.

similar structure was prepared within the TAPSim-MD framework, where an Al adatom was added on an ⟨111⟩ oriented Al substrate with a radius of 9 nm and height of 1.2 nm, large enough to eliminate field edge effects for the Al adatom in the center. We chose the rigorously validated interatomic potential from Mishin et al. [59]. Although the electric field cannot be directly controlled in TAPSim-MD, different electric fields can be obtained by manipulating the applied voltages. The chosen plot of force vs. z-position still allows a direct comparison of DFT and TAPSim-MD simulation despite the differences in the field control. As shown in Fig. 6 (c), force vs. z-position for the adatom is plotted for different applied voltages. For each set of simulations, the position of the adatom along the z-axis was increased by 0.1 Å per time step while the applied voltage was held constant.

As shown in Fig. 6, in both DFT and TAPSim-MD calculations, as the electric field or voltage increases, the distance between the equilibrium position (the first point where the force equals 0) and the position of the evaporation barrier (the second point where the force equals 0) decreases and eventually goes to zero. Also, inspecting the Ref. [23] and TAPSim-MD columns respectively, the shapes of the force curves under field stay consistent with the force curves in the absence of field (pure interatomic forces). The differences between the zero-field force curves of Ref. [23] and TAPSim-MD are mostly due to the finite interaction radius of the fitted potential, where neighbor shells that leave the interaction sphere cause undulations in the force curves. We also plotted the force minimum ($-dE/dz$ of the inflection point of the energy curve) vs. the corresponding distance to the equilibrium position in Fig. 7, where the data points were extracted from the force-vs.-position plots in Fig. 6 for different applied electric fields or voltages. A negative sign of the force indicates that its direction points toward the surface. As the

DISTRIBUTION A: Distribution approved for public release.

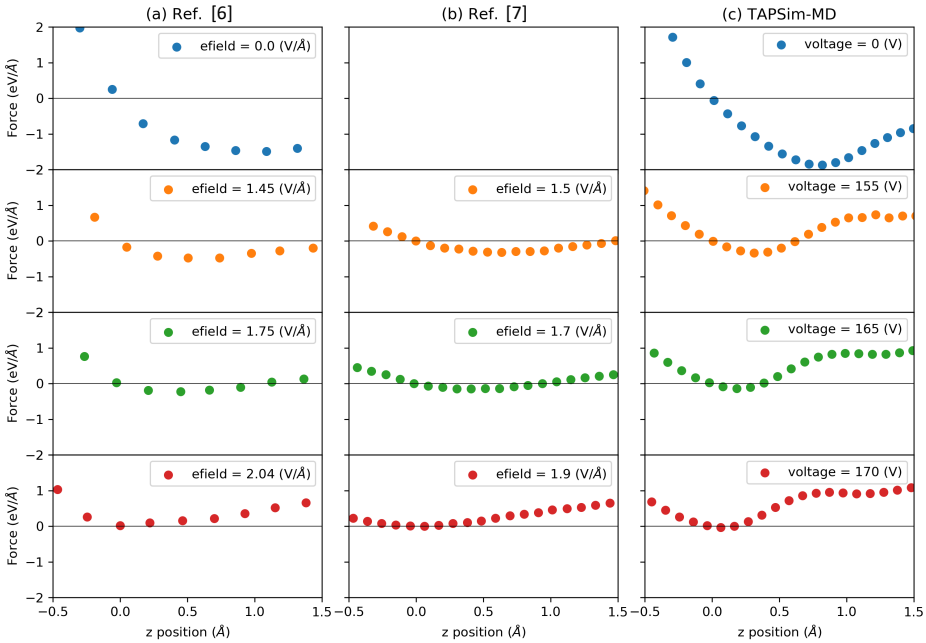

Figure 6: Force vs. distance from the equilibrium position of the evaporating adatom: (a) was derived from energy vs. distance in Fig. 4 of Ref. [23]; (b) was derived from energy vs. distance in Fig. 5 of Ref. [28]; and (c) was calculated by TAPSim-MD.

applied field or voltage increases, the evaporation energy barrier decreases, and the position of the force minimum gradually approaches the equilibrium position. Eventually, when the applied field or voltage is large enough, the evaporation energy barrier disappears, and these two positions overlap each other, resulting in zero distance and zero force in Fig. 7. This field then defines the zero-barrier evaporation field (ZBEF). If the field keeps increasing, the force minimum becomes positive, which means the force now points toward the vacuum space. As Fig. 7 shows, the magnitudes of the force minima found in TAPSim-MD simulations are well comparable to the DFT results. Focusing on the most important regions, the DFT data and TAPSim-MD data agree well at near zero distances (i.e., around the evaporation field). For lower fields (corresponding to larger distances), only Ref. [23] DFT data are available, where we find within 20% and 23% similar distance and minimum-force values as indicated by the green and blue arrows, respectively. Thus, as long as a carefully benchmarked interatomic potential is used, our method is adequate to predict evaporation sequences and atom trajectories reasonably well.

DISTRIBUTION A: Distribution approved for public release.

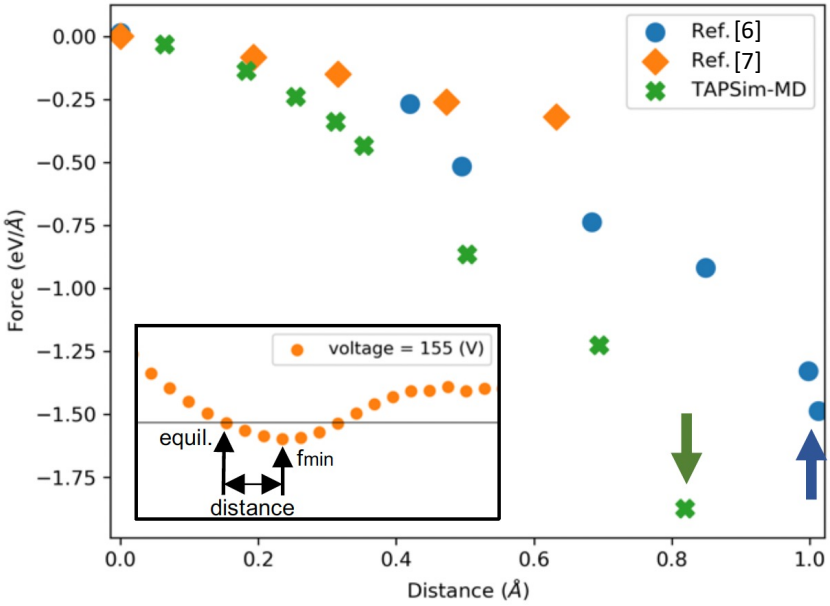

Figure 7: Minimum force vs. distance between the equilibrium position and the force minimum under different electric fields or voltages as indicated in the inset for curves of the type shown in Fig. 6. The negative force sign indicates a force pointing toward the surface. The blue arrow indicates the data point obtained with zero applied electric field in Ref. [23]. The green arrow indicates the data point obtained with zero applied voltage in TAPSim-MD.

5.5.4 Influence of Interatomic Potential on Simulations

As mentioned before, the selection of the interatomic potential is crucial to the MD simulation. To demonstrate its impact, we compare the results from two common EAM potentials [60, 61] for the Cu-Ni binary alloy system and assess the physical sensibility of their results.

The virtual tips for these simulations are cylinders with 4 nm in radius and 12 nm in height. Nine virtual tips were generated with randomly arranged Ni impurities with concentrations of 0%, 5%, 15%, 30%, 50%, 70%, 85%, 95%, 100%. Evaporation from these tips was studied with the interatomic potential by Foiles et al. [60] in comparison to the potential by Onat et al. [61]. The important difference between the potentials is that Foiles used two elemental EAM potentials where the cross term ϕ_{AB} of interactions between two species is defined as the geometric average of the elemental pair potentials, whereas Onat fitted a dedicated cross term for the alloy potential.

The critical voltages in the simulations with both potentials were determined when applied voltages hit respective plateaus. For an isomorphous system such as Cu-Ni, properties follow in general the mixing rule, which will also be shown to be the case for the high entropy alloy discussed in Sec. 5.6.3. As shown in Fig. 8, the Foiles potential

DISTRIBUTION A: Distribution approved for public release.

produces critical voltages that have a pronounced quadratic dependence on the composition, while the linear relationship as expected for an isomorphous system is reproduced by the Onat potential. Considering the nature of the cross potential as a geometric average in the potential from Foiles, the quadratic relation should simply originate from the number of bonds in a binary solid solution, which quadratically depends on the composition [62]. However, the potential from Onat shows a linear dependence consistent with general expectations, and our results in Sec. 5.6.3 for the miscible elements in the FeNiCrCoCu high entropy alloy also display a "mixed" critical voltage. Compared to the dedicated cross term fitted in Onat's potential, the definition of the cross term as the geometric average in Foiles's is too simplified to accurately describe interactions between Cu and Ni atoms, which is the reason why later alloy approaches in EAM do not use it anymore [12, 63, 64, 65]. Since the evaporation field of an atom is directly connected to its sublimation energy which in turn is closely related to its atomic neighborhood as was already recognized early in e.g., the "Müller formula" [22], a correct description of interatomic interactions is essential for obtaining reliable sublimation energies in describing field evaporation.

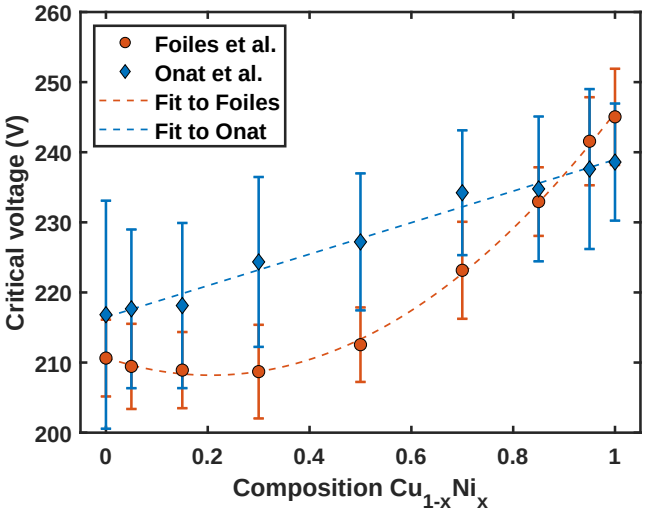

Figure 8: Critical voltages for $Cu_{1-x}Ni_x$ alloys obtained with interatomic potentials from Ref. [60] (Foiles) and Ref. [61] (Onat). Error bars represent the mean squared errors of the critical voltages.

From this case, it can be seen that field evaporation simulation provides an alternative way, albeit rather computationally intensive, of assessing the reliability of interatomic potentials. Another example involving selection of interatomic potentials will be given in Sec. 5.9, where we needed to identify an IAP that is appropriate for simulating evaporation of precipitates in Al-Cu alloys.

DISTRIBUTION A: Distribution approved for public release.

5.6 Basic Properties of Virtual Emitters

5.6.1 Steady-state Tip Shape

In APT experiments, the data collected until a steady-state tip shape is reached are usually discarded. Once the steady-state shape is reached, evaporation of the surface atoms happens typically layer by layer, resulting in a periodically returning tip morphology. Steady-state shapes of virtual tips are also observed in our simulations. Figure 9 includes snapshots of the steady-state shapes of tips of the three most common crystal structures for metals in $\langle 001 \rangle$ (or [0001]) orientation, bcc W, fcc Al, and hcp Ti. The size of the virtual tips is 4 nm in radius. The surface atoms are colored by the magnitude of the electric-field-induced forces (external forces). As expected, the field is concentrated on the edges of the atomic terraces. Therefore, the evaporation of surface atoms always tends to progress from the edges towards the center, which causes faceting. Moreover, the prominent lattice planes revealed by the top view of the tips in Fig. 9 follow the relative prominence rule that states that planes with the largest interplanar spacings are the most prominent [66]. For bcc, the most prominent planes are {110}, and the second prominent planes are {002}; for fcc, the most prominent planes are {111}, and the second prominent planes are {002}; for hcp, the most prominent planes are {0002}, and the second prominent planes are $\{1\bar{1}01\}$ (the most prominent planes in general should be $\{01\bar{1}0\}$, however they are the shaft surface of the cylinder, therefore are not considered here). In Fig. 9, we see indeed {110} and {002} for W, {111} and {002} for Al, and {0002} and $\{1\bar{1}01\}$ for Ti virtual tips as the most prominent planes, respectively.

5.6.2 Material-dependent Critical Voltage

The applied voltage in the previous TST-based simulation approaches does not have a quantitative meaning, since codes like TAPSim [41] evaporate atoms based on a local field-strength criterion such as the relative strength of the local field with respect to the tabulated evaporation field values of the respective chemical species, without considering the local bonding environment. Thus, the voltage is usually set to some reasonable value to create the electric field distribution, irrespective of the material examined.

In our approach, evaporation results from the competition between interatomic forces and field-induced forces, which gives a physical meaning and material dependence to the applied voltage. In order to trigger a single field evaporation event at a time mimicking a real experiment, the applied voltage is controlled to increase first rapidly by 10 V after a set of MD runs then slowly by 0.1 V until the first atom evaporates. After that, it is reduced successively by 0.1 V until no more evaporation events are detected, and ramped up by 0.1 V again until the next evaporation event happens. Figure 10 shows that after some initially high values which we call "over voltage" originating from the initially chosen tip shape, which will be discussed later in this section, the evaporation voltage oscillates around a constant value which defines the "critical voltage". Its value slightly decreases with decreasing tip height (keeping the field constant). Since the interatomic forces are determined from carefully fitted interatomic potentials and have realistic values, different materials with different bond strengths will require different

DISTRIBUTION A: Distribution approved for public release.

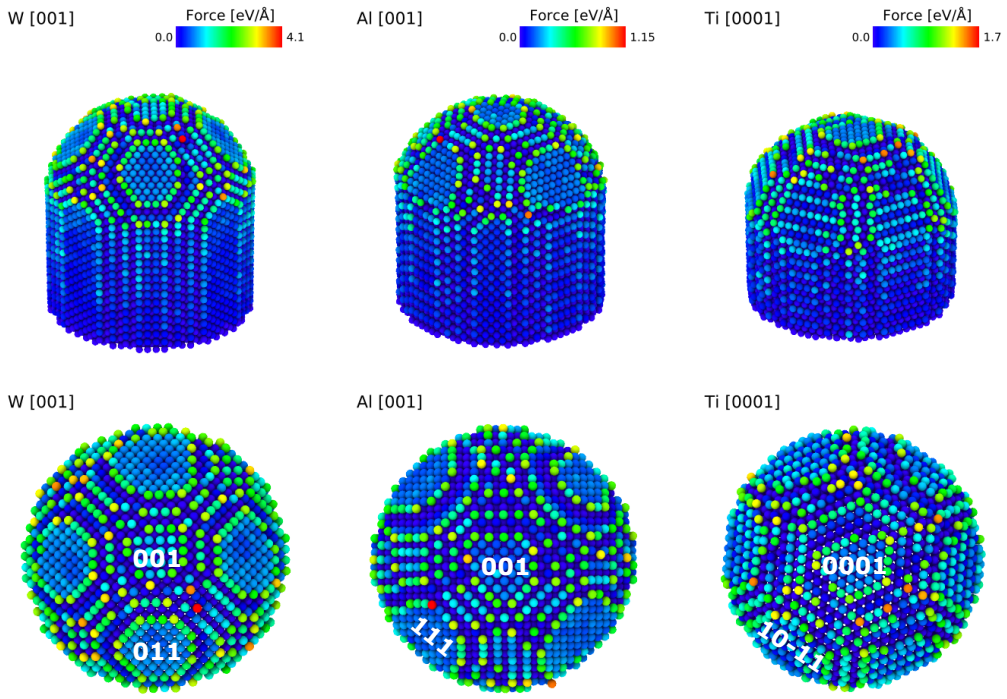

Figure 9: Steady-state tip shapes of different metals as labeled for virtual tips with 4 nm in radius. Surface atoms are colored by the magnitude of the electric-field-induced forces. The top view of the tips are displayed in the second row with the prominent facets labeled.

voltage values. Also, the same atomic species may require different voltage values when presents in different alloys or compounds where the atomic bonding strength changes and depends on their coordination. Thus, the critical voltage has a physical meaning and can be benchmarked against experimental observations.

Critical Voltage Results. The results in Fig. 10 are from virtual tips in the shape of a hemisphere on top of a cylinder to mimic the idealized shape assumed for classical reconstruction. The size of the virtual tips is 4 nm in radius and 12 nm in total height. The $\langle 001 \rangle$ direction of the tip ($\langle 0001 \rangle$ direction for HCP structure) is oriented along the z axis. Simulated elemental metals as shown in Fig. 10(a) include the fcc metals Al, Cu, Ni, and Au; hcp metals Co and Ti; and bcc metals W and Fe.

The sequence of critical voltages from high to low is W ($\sim$ 295.0 V), Ni ($\sim$ 241.5 V), Co ($\sim$ 215.3 V), Fe ($\sim$ 208.9 V), Cu ($\sim$ 184.4 V), Ti ($\sim$ 170.7 V), and Al ($\sim$ 137.6 V), which are obtained respectively as the averages of their voltages within the third quarter of the corresponding time ranges. The sequence of the tabulated ZBEF in Tsong's paper [38] from high to low is W (5.7 V/Å), Co (3.6 V/Å), Ni (3.5 V/Å), Fe (3.5 V/Å), Cu (3.0 V/Å), Ti (2.5 V/Å), Al (1.9 V/Å). Figure 11 shows a plot of the critical voltages vs. the tabulated corresponding ZBEF values from Tsong [38]. Except for Ni, which is somehow

DISTRIBUTION A: Distribution approved for public release.

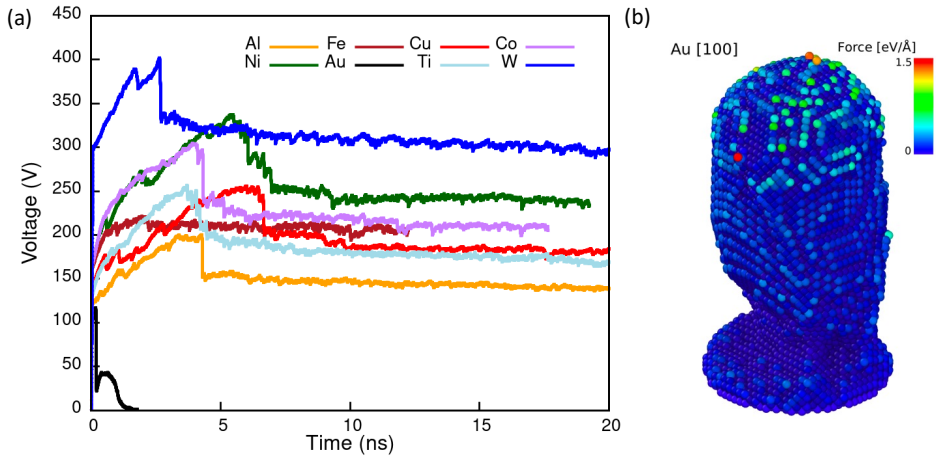

Figure 10: (a) Critical evaporation voltages of different metals. The hemispherical tip size is 4 nm in radius and 12 nm in total height. (b) An Au tip deforms during the simulation which leads to fracture. Surface atoms are colored by the magnitude of the electric-field induced forces.

an outlier, all other points lie nearly perfectly on a straight line, which is fitted here by the red line. From that, we can see that the critical voltage is directly proportional to the tabulated ZBEF with $V_{\text{crit}} = (40.8\ \text{Å}) \cdot \text{ZBEF} + 64.6V$. Thus, with the exception of Ni, the simulation results are not only in qualitative, but also in (scaled) quantitative agreement with the theoretical predictions, which is a first indication that the use of interatomic forces and field-induced forces is able to capture the basic features of field evaporation. The simulation of Au went to failure during the simulation as shown in Fig. 10(b) due to Au's high ductility and peculiar deformation mechanism, which also makes it very difficult to stabilize the pure gold specimen in experiment [67]. Although we successfully managed to fit a direct mapping between V_{crit} and ZBEF, it is in general not easy to convert the voltage value from the simulation to a corresponding ZBEF due to the geometry dependence of electric fields and the very different, much smaller geometry of the virtual setup in comparison to experiments. Nevertheless, we will show in Sec. 5.6.3 that average evaporation fields can be determined for various elemental metals in simulation and benchmarked against tabulated values in a more direct way.

Effect of Tip Shape on Critical Voltage. As can be seen in Fig. 10(a), there is a considerable over-voltage stage during the initial shape evolution that lasts a few ns, whose value is about 20% to 25% higher than the obtained critical voltage. We find that this over-voltage is closely related to the initial hemispherical tip shape and causes inefficiency in the simulation. Figure 12 is an example of a 4 nm-radius ⟨001⟩ oriented W tip starting with a hemispherical shape. The figure includes snapshots of the tip at 0.11 ns, 2.64 ns, 2.74 ns and 13.01 ns. Since the tip surface is hemispherical, there is no pronounced concentration of electric field on the surface in the beginning, as indicated

DISTRIBUTION A: Distribution approved for public release.

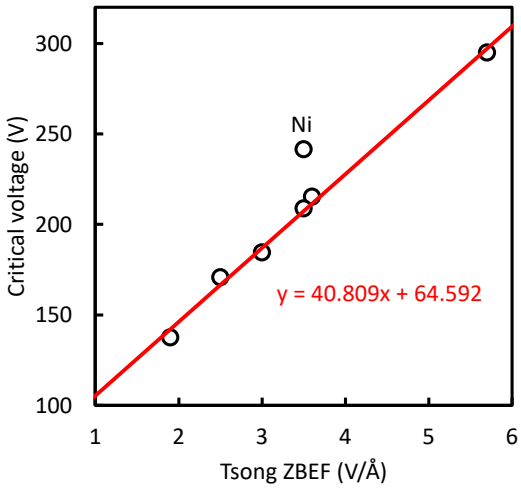

Figure 11: Critical evaporation voltages of different metals simulated (W, Co, Ni, Fe, Cu, Ti, and Al) vs. ZBEF values from Tsong [38]. The red line is a linear fit (equation shown in red) to all values except for Ni, which is treated as an outlier.

by the homogeneous coloring of the surface atoms observed up to 2.64 ns. In order to create higher local electric fields and trigger evaporation events, the voltage needs to increase. In this example, due to the stable hemispherical shape, although the voltage goes up considerably by about 34%, only about 1250 atoms are evaporated during the first 2.53 ns. However, during the following 0.1 ns, about 600 atoms are evaporated very quickly, which results in a very large {002} and some smaller {110} facets. The {002} terrace has a large edge where the electric field can concentrate, and the applied voltage drops promptly by about 17% within 0.1 ns approaching the critical voltage. The tip then evolves to a semi-stable shape as shown at 13.01 ns. Since this avalanche of atoms cannot be analyzed in a meaningful way, the initial computation wastes considerable computer time. The effect is exacerbated as the number of atoms ripped off in the avalanche is too large and results in a too-flat tip surface with a much smaller curvature compared to the steady-state shape, therefore more steps are required before the final tip shape is reached. In this example, the tip is not able to evolve to its steady-state shape shown in Fig. 9 before the whole tip is evaporated. Therefore, an initial hemispherical shape, while perhaps intuitive since close to the faceted steady-state shape, is highly inefficient.

In order to overcome this inefficiency, we found a cylinder tip with a flat end cap to be a much better initial structure. We demonstrate this for a ⟨001⟩ oriented Al tip with a 4 nm radius. We compare the evolution of the applied voltage between a cylindrical and hemispherical tip in Fig. 13. In contrast to the voltage applied to the hemispherical tip, the voltage applied to the cylindrical tip quickly reaches its critical voltage within about 2 ns, thanks to the concentration of electric field on the rim of the cylinder. Starting

DISTRIBUTION A: Distribution approved for public release.

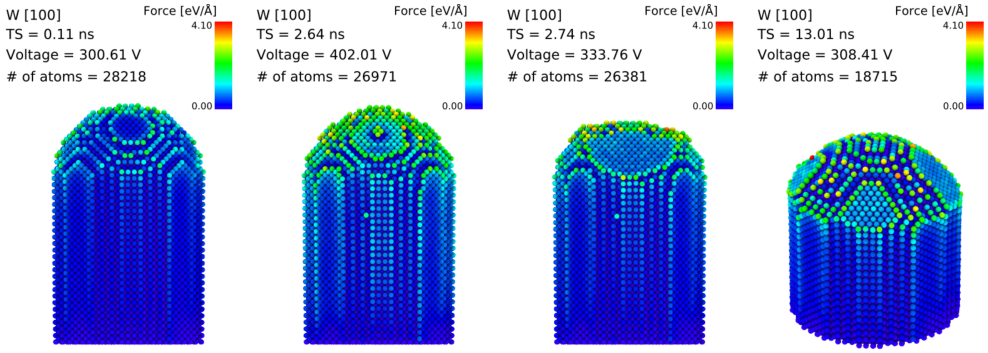

Figure 12: Evolution of a 4 nm-radius ⟨001⟩ hemispherical W tip. Surface atoms are colored by the magnitude of the electric-field-induced forces.

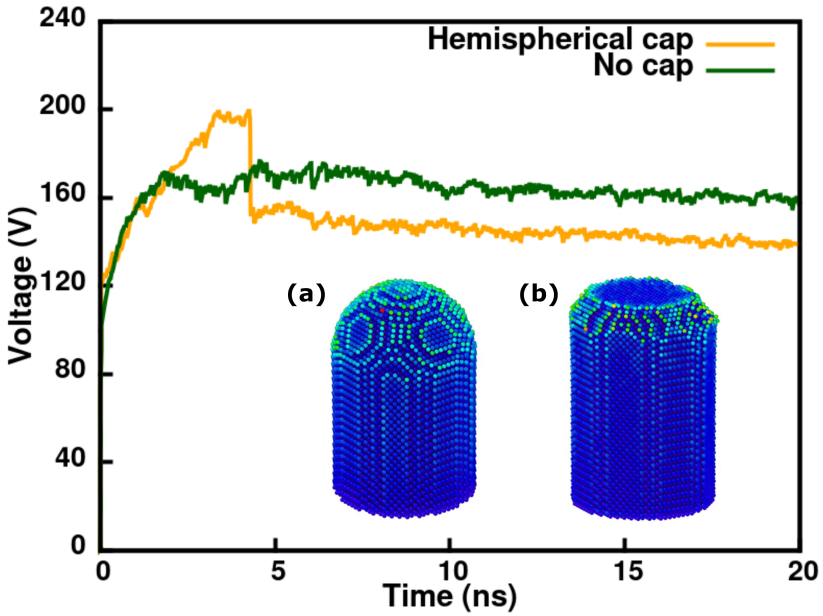

Figure 13: Applied voltage vs. time in hemispherical and cylindrical Al virtual tips. The tip structure of each case is (a) ⟨001⟩ oriented hemispherical tip and (b) ⟨001⟩ oriented cylindrical tip. The size of both tips is 4 nm in radius. Surface atoms are colored by the magnitude of the electric-field-induced forces.

from the edge, the tip gradually evolves to its steady-state shape. There is no "over-voltage" stage or avalanche-evaporation of atoms in this process and the steady-state shape is reached within short simulation time. Therefore we use cylinders as start shapes of virtual tips in all other simulations. As a side note, the different critical voltages were obtained in the two cases as a result of different tip heights when the voltages reach the respective plateaus. In addition, since a cylinder is distinctly different from the final steady-state shape, the consistent evolution of the tip shape to its steady state in

DISTRIBUTION A: Distribution approved for public release.

independent simulations further validates the present simulation method.

5.6.3 Critical Evaporation Field and Average Sublimation Energy

In this section, our goal is to derive critical evaporation fields of different elemental metals from simulation results and examine if they have a direct comparison to tabulated ZBEF data. In addition, in order to examine alloying effects in an extreme case, simulations are conducted in an fcc almost equiatomic FeNiCrCoCu high entropy alloy, which is later referred to as the FeNiCrCoCu HEA or HEA for simplicity. The HEA tip was cut from the periodic replica of a 32-atom special quasi-random structure (SQS) cubic cell with 6 Fe, 6 Cr, 6 Cu, 7 Ni and 7 Co atoms. The exact composition of the tip is 18.8% Fe, 21.9% Ni, 18.9% Cr, 21.8% Co, and 18.6% Cu. We compare the obtained sublimation energies to the tabulated data, as well as the sublimation energies and critical voltages for the different constituents in their elemental forms and in the HEA, where a "mixed" critical voltage of the HEA is found.

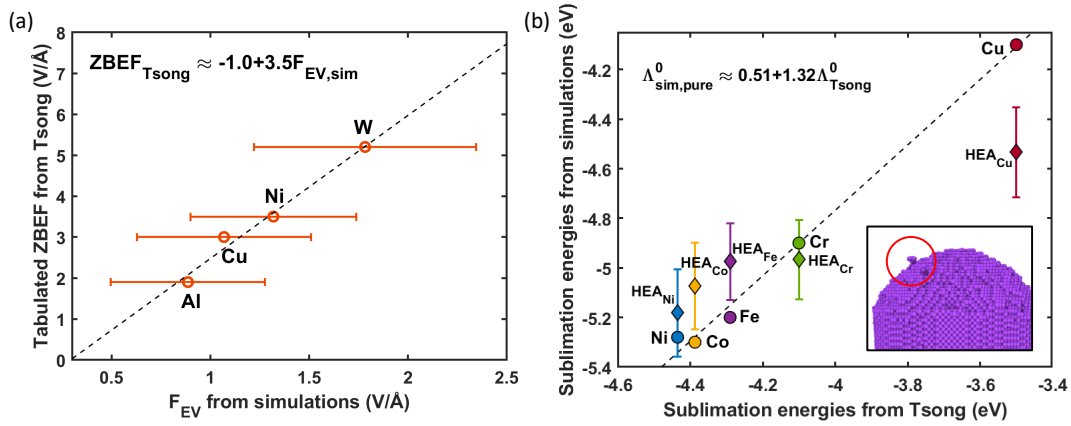

Figure 14: (a) Average critical evaporation fields of different elemental metals from simulations of virtual tips with 4 nm in radius vs. tabulated ZBEF values from Tsong [38]. The error bars represent the standard deviation of the observed evaporation fields. (b) Averaged sublimation energies of Co, Ni, Fe, Cu, and Cr metals in elemental forms (circles) and as components of an HEA (diamonds) vs. tabulated sublimation energies from Tsong [38]. Symbols in the same color represent the same species. The error bars represent the standard deviation of sublimation energies of components in the HEA. The virtual tips were 5 nm in radius and all simulations used the same interatomic potential. The inset is a snapshot of the tip surface during evaporation. An evaporating cluster is indicated by a red circle.

Although the local electric field is site-dependent for surface atoms, in order to compare to the tabulated ZBEF in Tsong's paper [38], the critical evaporation field is derived as an averaged value over all evaporation events. The local electric field of an evaporated atom is chosen as its critical evaporation field at the time when its interatomic force

DISTRIBUTION A: Distribution approved for public release.

goes to zero. As shown in Fig. 14(a), typical tabulated ZBEF values [38] are about 3.5 times higher than the critical electric field obtained in our simulations. Since the aberration is systematic, it demonstrates that while the reduced scales of the MD setup cause some scaling in potentials and fields, the process of evaporation is described with high fidelity where a linear dependence is found between simulated and calculated values. This conclusion is also supported by the excellent correlation between critical voltage and tabulated ZBEF values that we have shown in Fig. 11, where however Ni was found to be an outlier. In comparison, Ni is perfectly within the trend in Fig. 14(a), where the local electric field is correlated to the ZBEF values rather than the critical voltage as was done in Fig. 11, suggesting that Ni was evaporated at a different rate from the other metals before the steady state was achieved, and thus the different remaining tip height resulted in an artificially enhanced apparent critical voltage, which is much more pronounced in our simulations than in experiment since the virtual detector is very close to the tip. This also indicates that it is important to assess evaporation fields from the local field strengths during evaporation rather than from the overall critical voltages, which are susceptible to artifacts such as this one.

A similar analysis of local critical fields has also been done for zero-field sublimation energies of surface atoms of the FeNiCrCoCu HEA cylinder tip. Simulations were performed for the HEA tip of 5 nm in radius as well as for elemental metals of each alloy component using the same interatomic potential. Sublimation energies were computed for $\langle 001 \rangle$ surface atoms. In Fig. 14b, circles are results obtained for elemental metals of HEA components, while diamonds are obtained in the HEA alloy. Symbols of the same element are in the same color. Sublimation energies of elemental metals are very close to each other in the case of Co, Fe, and Ni, whereas Cu bonds are much weaker than the others. Compared to the homogeneous bonding environment in the elemental metals, there is a distribution of sublimation energies for each of the components in the HEA as shown in Fig. 14(b), which indicates a mixing effect caused by different bonding contributions from different neighbor atoms. Average sublimation energies of each component in the HEA have a similar sequence compared to the elemental metals, however, the discrepancy of the bond strength among components is mitigated. The standard deviation of sublimation energies of the elemental metals is 0.50 eV, while that of the HEA atoms is only 0.28 eV. The trend of homogenization of bonds is also reflected in the critical voltage. As shown in Tab. 1, the critical voltage of the HEA nearly equals the average of the critical voltages of elemental metals of the components following the rule of mixture, which is an important result that we have used in Sec. 5.5.4 in the case of Cu-Ni alloy to discuss the assessment of the reliability of interatomic potentials.

Although a homogenization effect of bonds is observed in the HEA, the copper atoms still have the weakest bonds among the alloy components, and their average sublimation energy has the largest deviation of -8.3% from the average of -4.95 eV of all atoms in the sample. In contrast, the deviations of Ni, Co, Fe and Cr are 4.8%, 2.6%, 0.59% and 0.42% respectively. The much weaker bonding of copper atoms makes them the easiest ones to evaporate in the HEA, and their preferential evaporation causes a rough tip surface with dimples and evaporation of clusters (separation at the "weakest link", see the inset in Fig. 14(b)). With our carefully controlled voltage-driven evaporation,

DISTRIBUTION A: Distribution approved for public release.

we never observe cluster evaporation in elemental metals. This finding explains and is in agreement with experimental observations in a similar, compositionally homogeneous equiatomic FeNiCrCoMn HEA, where in voltage mode an unusually high fraction of 30%-40% multiple vs. single hits is observed [68], which is more than an order of magnitude larger than what is typically observed for elemental metal tips [69].

Table 1: Comparison of elemental vs. alloy critical voltages of components of the $Fe_{18.8}Ni_{21.9}Cr_{18.9}Co_{21.8}Cu_{18.6}$ high entropy alloy.

Component	Ni	Cr	Co	Fe	Cu
Concentration (%)	21.9	18.9	21.8	18.8	18.6
Critical voltages of elemental metals (V)	342.1	317.0	311.4	284.0	242.7
Weighted average of critical voltages (V)				301.2	
Critical voltage of HEA (V)				298.4	

As a final note, we do not observe any recognizable zone lines or poles in the evaporation map of the HEA. This agrees with the general expectation, since for example in highly alloyed steels, zone lines and poles start to wash out and disappear with an increasing solute concentration [70, 71, 72]. However, at this point, we cannot make any comparison to experiments so far, as no evaporation map of HEA has been reported in the literature.

5.7 Origin of Enhanced Zone Lines in Field Evaporation Maps

5.7.1 Background

As introduced in Sec. 5.1, field evaporation maps, which are the cumulative images of all atom impacts, often exhibit depleted poles, concentric ring patterns, and depleted or enhanced zone lines connecting poles. While reasonable explanations exist for most of the features observed in field evaporation maps, for example, depleted zone lines [3], the enhanced zone lines have yet to be explained conclusively. The most widely believed hypothesis about their origin may be the so called "roll-up" mechanism proposed by Waugh et al. in 1976 [73], where the evaporating atom at a terrace ledge "rolls" up over the plane edge and is channelled by its neighbors in a specific direction towards the plane center.

Since it is impossible to study the formation of evaporation maps experimentally due to the intrinsic destructiveness of field evaporation, forward modeling has been suggested as the most viable way to investigate this process [3, 39]. However, even the most advanced classical electrostatic methods developed for APT modeling such as TAPSim [41], are not able to reproduce enhanced zone lines. In contrast to the experimental evaporation map of a $\langle 110 \rangle$ oriented tungsten tip in Fig. 15(a), the TAPSim result in Fig. 15(b) only shows broad and depleted stripes around zone lines. Similar results have been reported using other classical electrostatic models [3, 40, 43]. As mentioned in Sec. 5.3, such modeling approaches are all based on the transition state theory (TST), and therefore are not able to describe any dynamic details about how atoms leave the surface. Thus,

DISTRIBUTION A: Distribution approved for public release.

the pattern of enhanced zone lines should be associated with full dynamics, as it cannot be reproduced and explained by the TST-based models.

The simulation approach implemented in the "TAPSim-MD" code introduced in the present thesis and in Ref. [53] includes the full dynamics and thus overcomes the limitations of the previous TST-based models by integrating field evaporation as part of the MD simulation. As described in the previous sections, the evaporation process is triggered by increasing the applied electric field to a point after which the electrostatic forces stay stronger than the interatomic forces. For convenience, we will use "external" and "internal" forces to refer to electrostatic and interatomic forces in the discussion. Unlike the classical TST-based approaches, we do not halt the MD at the moment of evaporation and send the atom with zero initial velocity into the trajectory simulator. Instead, the atom velocity is a continuous function resulting from the forces acting on it. We will show using the canonical example of tungsten that this velocity includes a lateral component resulting from the misalignment of external and internal forces, which deviates the atom trajectories towards certain directions and gives rise to enhanced zone lines on the evaporation map.

5.7.2 Simulation and Experimental Details

TAPSim-MD simulations in three virtual W ⟨110⟩ tips at 50 K with 8 nm, 10 nm and 15 nm in radius are used for our analysis, where the different sizes offer different advantages for specific analyses but fundamentally show analogous results. A test of convergence of the evaporation map vs. tip size finds that tip sizes of 8 nm are sufficient to produce a converged evaporation map pattern. Since this size starts to become intractable with the previous voltage change protocol described in Sec. 5.6.2, we adopted a different protocol here which uses the field as bias to accelerate the infrequent events of evaporation in the spirit of accelerated dynamics [74], which then allows to run larger tips. The new protocol only increases the applied voltage and never decreases it, and also uses larger increments. This causes a higher evaporation rate and frequently simultaneous evaporation of several atoms, which however is no problem in simulation since detection of evaporation events is independent of how many atoms evaporate simultaneously. Such an optimized protocol for the example of an 8 nm-radius 24 nm-height W tip then looks like this: To increase the voltage, we first set a large increment of 20 V ("voltage_ramp_up=20") after a set of MD runs until 650 V ("voltage_ramp_to=650"), where nothing should happen, and then set a small increment of 8 V ("voltage_up=8") after a set of MD runs for a finer control until an atom gets evaporated. As described in the new protocol, the voltage is set to never decrease ("voltage_down=0"). The voltage will then stay at the same level as long as it is high enough to trigger evaporation. The voltage will only increase when there is no more evaporation event occurring. The same voltage change protocol will be applied in the following sections including Sec. 5.8 and Sec. 5.9.

The most detailed evaporation pattern is obtained from the largest tip we can simulate at present with the accelerated voltage protocol, and thus the evaporation map shown in Fig. 15 comes from the 15 nm-radius tip. For analyses that require one-by-one inspection and a manageable overall number of atoms, the 8 or 10 nm-radius tip is used. About

DISTRIBUTION A: Distribution approved for public release.

30 layers of atoms are used in the 8 nm analysis, and 52 layers for the 10 nm tip. The interatomic potential of tungsten is of the modified embedded atom method type as parameterized by Marinica et al. [75]. For comparison of evaporation maps, we also performed a traditional TAPSim simulation for a 15 nm-radius W ⟨110⟩ tip with default settings. Details about TAPSim approach and applications can be found in Refs. [41, 76].

The experimental evaporation map was obtained from a W needle using a LEAP 3000HR. The needle was electropolished using a solution of 5% NaOH in water. During evaporation, the needle was maintained at a temperature of 60 K and evaporated using 15% pulse fraction, a pulse frequency of 200 kHz, and an evaporation rate of 0.002 atoms/pulse.

5.7.3 Results and Discussion

Figure 15 shows our simulated field evaporation map in (c) of the 15 nm-radius W tip in comparison to experiment in (a) and traditional TAPSim simulation in (b). The size of the virtual tip with 15 nm in radius is close to the experimental tip size of 17 nm in radius, which makes the results directly comparable. Our TAPSim-MD results reproduce the depleted pole center and enhanced zone lines consistent with experiment, where the intensity of atom hits is higher around the ⟨111⟩ and ⟨100⟩ zone lines, while zone lines simulated by the traditional TAPSim approach are depleted with a lower intensity of hit events.

The presence of the enhanced zone lines in our simulation makes it now possible to examine their origin. Figure 15(d) shows an evaporating atom along its initial trajectory, with vectors representing directions and magnitudes of external forces (blue) and internal forces (orange). As the atom pulls away from the surface under the effect of the applied external field, the interatomic force decreases while the external force grows.

While it has been previously suggested that evaporation should be seen as the result of the competition between interatomic and electrostatic forces [77], codes that have electrostatic forces act on a rigid tip imply that the internal, interatomic forces can be neglected in comparison to the external, electrostatic forces, which then become the sole drivers for evaporation events. In this approximation, the atom should be evaporated very quickly by the dominating external force, and the internal force would have little impact on the atom trajectory. Along with that, it is often assumed that the initial velocity component not parallel to the field would solely stem from thermal motion and have negligible effects on the detector image except for some minor blurring [78, 79, 80]. With regard to lateral precision and accuracy, the deviations from the ideal projecting directions have been attributed to trajectory aberrations, “aiming errors”, caused by geometry-related local field variations (which would be included in codes like TAPSim), local structure dependence of evaporation fields [22], or atomic motion, i.e. surface migration [81] or “roll-up motion” [73, 80]. In the following, we will show that by performing MD simulations considering both interatomic and electrostatic forces, these assumptions about field evaporation can be eliminated. We show specifically for the case of enhanced zone lines how initial velocity components not parallel to the field originate

DISTRIBUTION A: Distribution approved for public release.

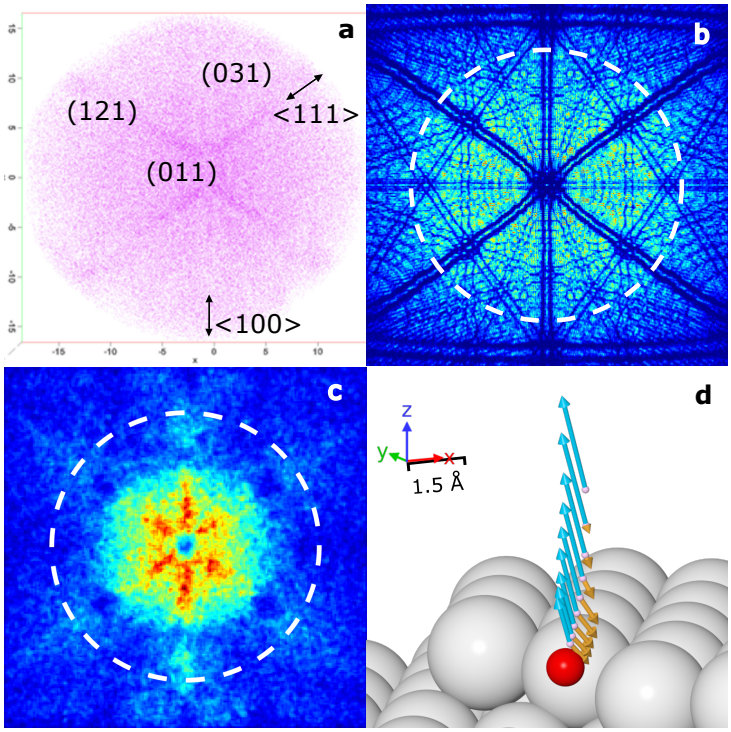

Figure 15: Field evaporation maps obtained for ⟨110⟩ oriented W tip in (a) experiment (tip radius = 17 nm); (b) traditional TAPSim simulation (tip radius = 15nm); (c) TAPSim-MD simulation (tip radius = 15 nm). The dashed circles in (b) and (c) indicate a field of view similar to the experimental evaporation map in (a). (d) Example atom trajectory during field evaporation. The evaporating atom is indicated by red (initial position) and pink (snapshots along trajectory) balls. Blue/orange arrows represent external/internal forces.

from the interaction between the two forces and eventually become responsible for the enhanced zone lines.

The external force induced by the local electric field depends on the local surface morphology and is in general approximately normal to the surface as shown before in Fig. 5. At the same time, the magnitude and direction of the internal force on an atom are determined by the interactions with its nearest neighbors and therefore depend on their configuration. Instead of directly diving into the analysis of forces, we therefore begin by analyzing the nearest neighbor configurations of the evaporating atoms. For that, we consider the first two nearest neighbor shells (NNs), since in the body-centered-cubic (bcc) lattice, the first and second-nearest neighbor distances are very close to each other as shown in Fig. 16a. In addition, we only focus on NNs in the same layer perpendicular to the sample axis as the evaporating atom, since we find that the layer beneath an evaporating atom is always large enough that the NN configurations in the layer beneath are identical for all evaporating atoms.

DISTRIBUTION A: Distribution approved for public release.

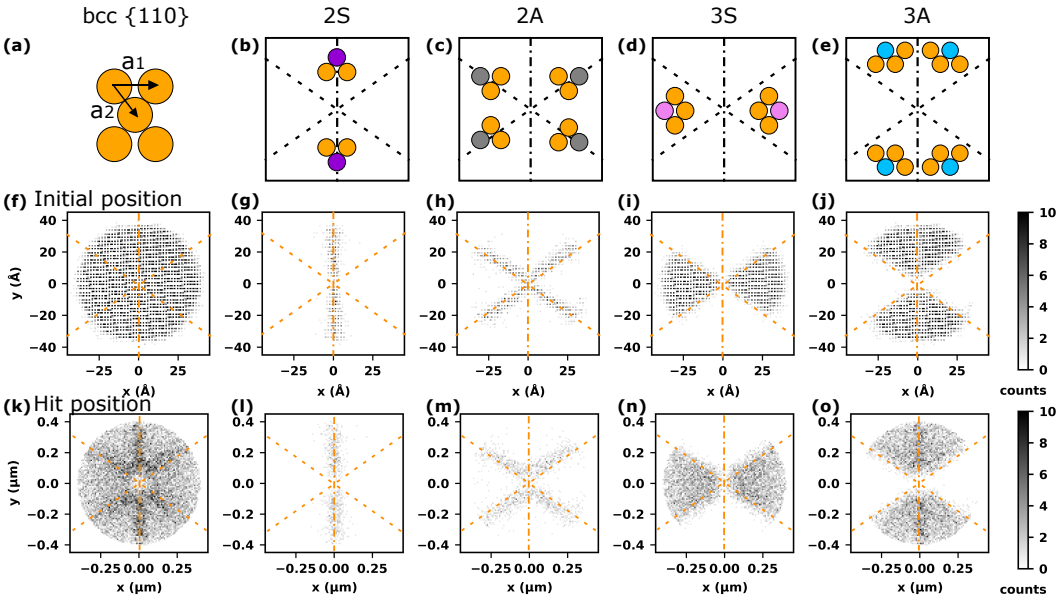

Figure 16: (a) is the geometry of bcc {110} plane, where a_1 is the lattice constant, $a_2 = 0.866a_1$; (b)-(e) are 4 classes of atoms categorized by NN configurations (evaporating atoms of each class are colored purple, gray, pink and blue respectively, neighbor atoms are colored orange); (f)-(j) are 2D histograms of (x,y) coordinates of all and each class of atoms in the virtual tip (initial positions); (k)-(o) are 2D histograms of detector hit positions of all and each class of evaporated atoms. The intensity of events of the 2D histograms is colored on a gray scale. The darker region has a higher intensity of events. Dashed lines represent $\langle 111 \rangle$ zone lines. Dash-dotted lines represent the $\langle 100 \rangle$ zone line. Data are from the simulation of the 8 nm-radius virtual tip.

As shown in Fig. 16(b)-(e), we categorize evaporated atoms into 4 classes based on the configurations of their NNs just before their evaporation, which are 2S, 2A, 3S and 3A. The number is the count of NNs in the same layer (atoms with 2 NNs are commonly known as step adatoms, with 3 NNs as kink atoms; atoms with NN $>$ 3 were not found to evaporate in our simulations), and the letter describes the symmetry of the configuration ("S" for symmetric and "A" for asymmetric). Atoms in the same class have the same NN configuration, which means their internal forces are in equivalent directions. Figure 16(g)-(j) show the distribution of initial (x, y) positions of evaporated atoms in each of the classes. It is evident that there is a strong correlation between NN configurations of evaporating atoms and their initial positions on the evaporating surface: atoms in 2S are located on the $\langle 100 \rangle$ zone line; atoms in 2A are located on $\langle 111 \rangle$ zone lines; atoms in 3S are mostly located between two $\langle 111 \rangle$ zone lines; atoms in 3A are mostly located between $\langle 111 \rangle$ and $\langle 100 \rangle$ zone lines.

The site-dependent NN configuration implies a certain sequence of the evaporation events. The atoms in a terrace edge before evaporation usually have three neighbors,

DISTRIBUTION A: Distribution approved for public release.

thus evaporation starts with those (see Fig. 17(a)). Faceted edges consist of a straight row of atoms with 3 or 4 NNs (see e.g. the row of atoms below atom g in Fig. 17(a)). If an atom has only 2 NNs at the time of evaporation such as atoms a, b or g in Fig. 17(a), they are the last ones evaporated in their rows. The atoms with 2 NNs are mainly located around $\langle 111 \rangle$ and $\langle 100 \rangle$ zone lines as indicated in Fig. 16(g) and (h), which implies that atoms located around these zone lines are the last ones to leave the corresponding edges. The same conclusion can also be made from the evaporation map obtained by the classical TAPSim method without considering any interatomic interaction in Fig. 15(b), where a narrow distribution of atoms is located in the middle of the zone lines indicating they are the last ones to leave the edges of the terraces. The simulation results from both approaches are in agreement with previous observation in field-ion images where atoms on $\langle 111 \rangle$ and $\langle 100 \rangle$ zone lines were reported to be the last ones to evaporate [73]. Both experiment and simulation confirm that the evaporation sequence is a consequence of the crystallography of the material.

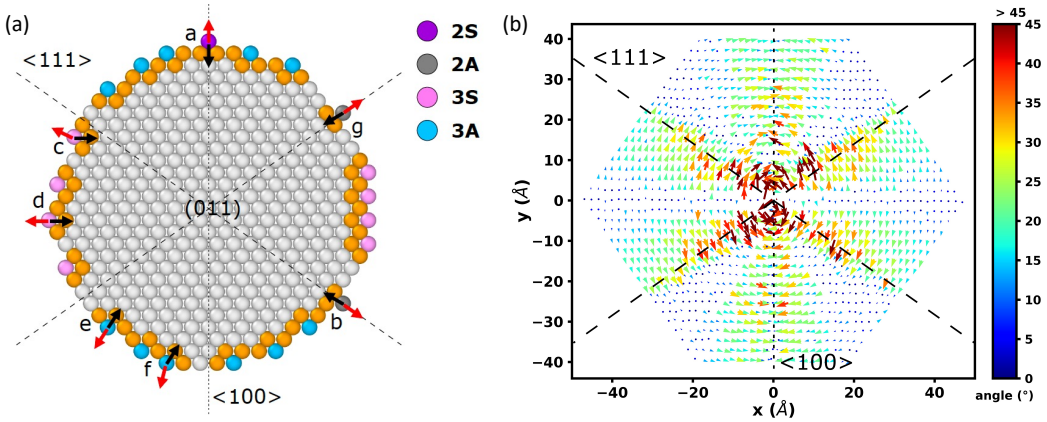

Figure 17: (a) Column-averaged transverse component of launch velocities in the xy-plane. Vectors are colored by the angle between the launch velocity and external force. (b) Representative (110) terrace including the 4 classes of evaporating atoms. Evaporating atoms are colored pink, gray, blue and purple; neighbors are in orange. Theoretical directions of lateral external (red) and internal (black) forces are sketched for atoms a-g. Dashed (dotted) lines represent $\langle 111 \rangle$ ($\langle 100 \rangle$) zone lines.

After grouping the evaporating atoms into four classes by their NNs, we now examine the respective resultant forces. Since the shape of the atomic terraces stays the same except for shrinking during evaporation, the local NN topology and the resulting directionality of both external and internal force are preserved in the given angular segments throughout the entire evaporation sequence. Figure 18(a) shows the distribution of the lateral components of external and internal forces of evaporating atoms in the four classes. Because all four quadrants are symmetry equivalent, forces are mapped to the first quadrant of the xy-plane where $x, y > 0$, to include more data for statistical analysis. The distinct nature of each of our four NN classes becomes more clear when

DISTRIBUTION A: Distribution approved for public release.

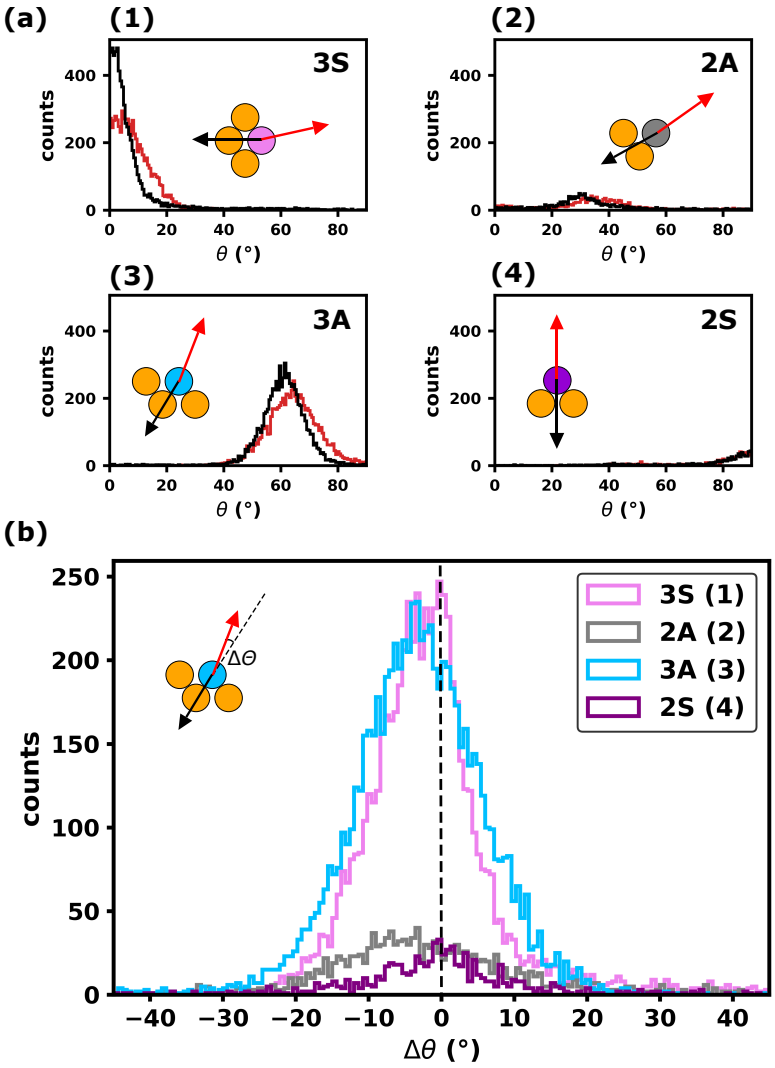

Figure 18: (a) Histograms of polar angles of the lateral external (red) and internal (black) forces of evaporating atoms in an 8 nm-radius tip in the 4 classes as labeled, which are mapped to the first quadrant. The evaporating atoms are colored pink, gray, blue and purple. Neighbor atoms are colored orange. (b) Histogram of the anti-alignment angle $\Delta\theta$ of the two forces. The definition of $\Delta\theta$ is illustrated by the inset.

looking at sub-panels (1)-(4) of Fig. 18(a), where each NN class has a well defined distribution of internal and external force directions of evaporating atoms in the xy-plane. The preferential directions of internal and external forces with major peaks around 0 and 60° and minor peaks around 30° and 90° can be explained by the directional distribution of the atoms in the four categories as shown in Fig. 16(g)-(j).

While the distributions of internal and external forces may look similar at first glance,

DISTRIBUTION A: Distribution approved for public release.

one can clearly see in Fig. 18(a) that for the two main peaks, (1) for 3S and (3) for 3A, the internal forces shift to the left of the external force peaks by about 5°. To quantify this shift better, we calculate for each atom the anti-alignment angle $\Delta\theta$ between internal and external forces as defined in the inset of Fig. 18(b). Indeed there is an angle misalignment between the external and internal force for most atoms. Except for the almost symmetrically distributed class 2S with mean position at -0.65°, peaks of class 3S, 2A and 3A all shift negatively from 0 whose mean positions are at -1.8°, -2.1° and -3.2° respectively. Since evaporation happens when the external force balances and starts to overcome the internal force, the resultant total force is close to zero. With that, the transverse force component from the misalignment is not a small distortion of the total net force but large enough to accelerate the atom in a direction deviating from the local field.

As shown in Fig. 17(b), the misalignment between the external and internal force causes a major lateral motion transverse to the local field towards the ⟨111⟩ and ⟨100⟩ zone lines, and away from the central (011) pole. For illustration of the link between neighbor arrangement and transverse acceleration, we look at a subset of evaporating atoms of the four classes on a representative (011) terrace with typical force alignment in Fig. 17(a). For atom c in class 3S, the misalignment between the two forces gives rise to a component of net force transverse to the external force (local field) pointing towards the ⟨111⟩ zone line. For atom f in class 3A, the misalignment deviates it towards the ⟨100⟩ zone line. For atoms a, b, d, e and g, their external and internal forces are more or less aligned, therefore little deviation is expected. The comparison between Fig. 17(a) and Fig. 17(b) shows that the 3S atoms accumulate around the ⟨111⟩ zone lines on the detector, whereas the 3A atoms enhance the ⟨100⟩ zone line. This result is also consistent with the 2D histogram of detector hit events in Fig. 16(k)-(o). Indicated by a darker color, the enhanced ⟨111⟩ zone lines shown in Fig. 16(k) are results of overlay of class 2A (Fig. 16(m)) and 3S (Fig. 16(n)), whereas the enhanced ⟨100⟩ zone lines result from overlay of class 2S (Fig. 16(l)) and 3A (Fig. 16(o)).

Similar effects have also been observed in simulations of tungsten 8 nm tips in different orientations. As shown in Fig. 19, the evaporation maps obtained for different orientations all have enhanced ⟨111⟩ and ⟨100⟩ zone lines, which is consistent with the experimental results. This consistent feature of enhanced zone lines demonstrates that: (1) faceting and the shape of each facet do not change with the orientation of the tip; (2) atom trajectories are deflected towards zone lines as a result of the misalignment between the electrostatic force and the interatomic force, regardless of the orientation of the tip. The enhanced zone lines have also be found in simulations of other metals, for example FCC Ni as shown in Fig. 20(c), which have a good agreement with experimental observation in Fig. 20(a), but cannot be reproduced by traditional TST-based approaches as shown in Fig. 20(b).

In conclusion, we answered the long-standing question about the origin of enhanced zone lines in field evaporation maps which could not be reproduced by previous TST-based simulation approaches and left explanations to non-quantitative *ad hoc* models such as Waugh's roll-up conjecture [73]. By using an "*ab initio*" approach to simulate field evaporation [53], we successfully reproduce this pattern and can show now for the

DISTRIBUTION A: Distribution approved for public release.

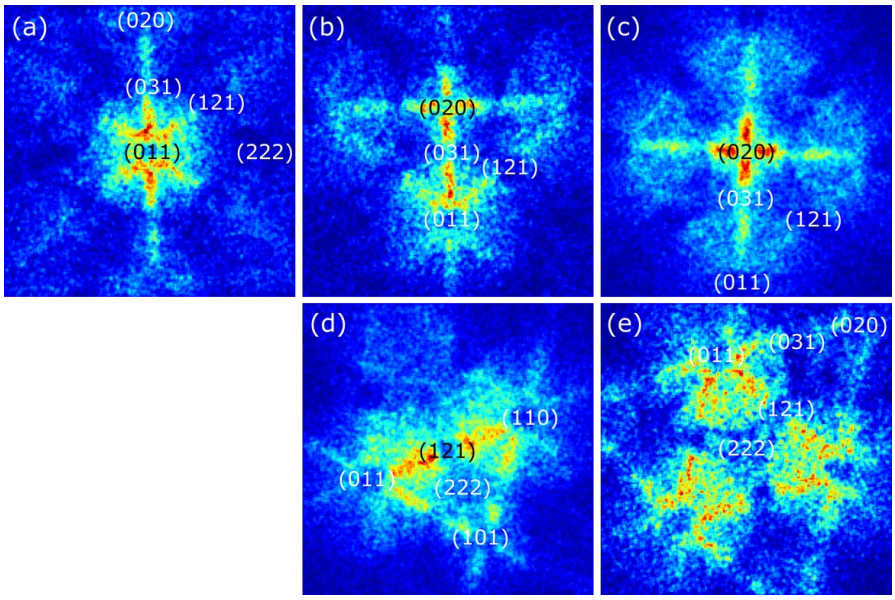

Figure 19: Evaporation maps for W tips of size of 8 nm in radius in different crystallographic orientations: ⟨110⟩, ⟨130⟩, ⟨100⟩, ⟨121⟩, ⟨111⟩.

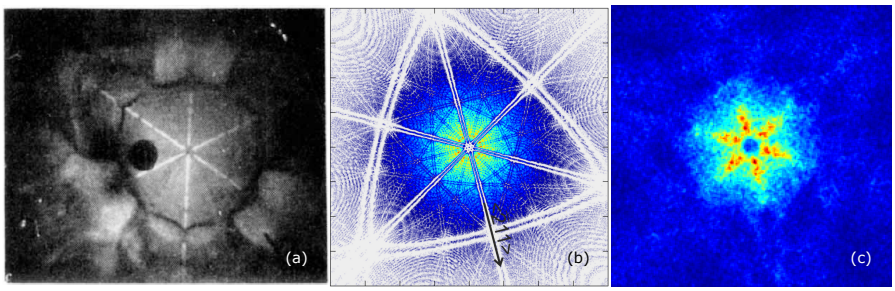

Figure 20: Field evaporation maps obtained for an ⟨111⟩ oriented Ni tip in (a) experiment, the figure is reprinted from Ref. [82]; (b) TAPSim simulation for an fcc ⟨111⟩ oriented structure (tip radius = 25 nm), the figure is reprinted from Ref. [76]; (c) TAPSim-MD simulation (tip radius = 8 nm).

canonical example of a ⟨110⟩ oriented tungsten tip that the magnitudes of interatomic forces and field-induced forces are comparable during the evaporation process. The possible misalignment of the two forces deviates the trajectory of the evaporating atom from its local field and causes accumulation of detector hit events around certain zone lines, which explains the observed enhanced zone lines.

5.8 Unexpected Field Evaporation Sequences in TiAl

As outlined in Sec. 5.1, the conventional reconstruction protocol operates under the assumption that the evaporating specimen maintains a perfect hemispherical shape, imply-

DISTRIBUTION A: Distribution approved for public release.

ing an ideal sequence for atom evaporation from the surface. However, the evaporation behavior observed in materials with layered structures often deviates from this ideal and involves distinct evaporation preference for different layers, where one layer tends to adhere to the surface while the other evaporates readily [5]. Traditionally, this behavior has been explained through a qualitative argument involving different evaporation fields, which disrupt the anticipated ideal evaporation sequence. This disturbance leads to the reconstruction of crystallographic planes at seemingly "incorrect" heights. In this section, we will perform an in-depth examination of this hypothesis, using the γ-TiAl intermetallic compound as a case study, which is a layered crystal with $L1_0$ structure.

5.8.1 Background

γ-TiAl is an excellent system for examining uncertainties in observed layer sequences in APT, since experimentally it is found that the reconstructed structure of [001] oriented TiAl tips has clearly separated, but mixed Ti/Al planes as shown in fig. 21(c), instead of alternating Ti- and Al-planes as one would expect from the crystal structure (Figure 21(a)) [83, 84, 85]. Based on field ion microscopy results, most of the literature concludes that Al tends to stick to the surface while Ti in the layer beneath evaporates readily, which is interpreted as Ti having a lower evaporation field than Al in TiAl [86, 87, 85]. This conclusion comes from the observation that Al is typically found to constitute the top layer, while the Ti-layer just beneath it is only slightly larger than the Al top layer but much smaller than the following Al layer as shown in Fig. 22(a). However, Lefebvre et al. came to the opposite conclusion of Ti having the higher evaporation field based on their observation that along the analysis direction, Ti planes were always immediately followed by Al planes [84]. Subsequently, Boll et al. performed simulations in order to reproduce their own experimental observation of Ti evaporating easier [88]. In order to reproduce this conclusion, they used Müller's formula from Eq. 12 for the evaporation field, from which they state to have found a higher evaporation field for Al when assuming for both Al and Ti a +2 charge state as they observed in experiment. However, their calculated evaporation fields are not reported in the paper, and it is not possible to reproduce them since the bond energy Λ of Ti-Al used to calculate the sublimation energy is $\Lambda_{\mathrm{Al-Ti}} = 0.70$ eV. Compared to the energies of the homoelemental bonds, $\Lambda_{\mathrm{Al-Al}} = 0.33$ eV and $\Lambda_{\mathrm{Ti-Ti}} = 1.07$ eV, the value of 0.70 eV results in an ordering energy of zero, which suggests Ti and Al to form an ideal solid solution and not an ordered intermetallic. Our own DFT-values for these bond energies reported in Sec. 5.8.3 are in stark contrast to either value, with $\Lambda_{\mathrm{Al-Ti}} = 0.86$ eV, $\Lambda_{\mathrm{Al-Al}} = 0.58$ eV, and $\Lambda_{\mathrm{Ti-Ti}} = 0.91$ eV and an ordering energy of -0.12 eV in the common range of intermetallics.

In order to sort through these contradictory findings, we revisit here the field evaporation sequence of [001]-oriented TiAl by applying the full-dynamics field evaporation simulation approach introduced in this thesis, TAPSim-MD [53]. As discussed in Sec. 5.4.3, our approach evaporates atoms in the specimen as a result of competition between interatomic forces and electrostatic forces, and gives an "*ab-initio*" prediction of evaporation events as well as atom trajectories. Here for the example of [001]-oriented TiAl, we show

DISTRIBUTION A: Distribution approved for public release.

that without any knowledge of charge states, TAPSim-MD successfully reproduces the "pair" pattern of the surface morphology and the mixed-layer reconstructed structure. Our results suggest that Al indeed possesses a higher evaporation field than Ti, which is in agreement with most previous conclusions from experiments. However, in contrast to previous suggestions, we find from analyzing the atomic trajectories that Ti is preferentially evaporated due to its two-step bond breaking process, which is easier to happen in comparison to the evaporation process for Al, where all bonds are simultaneously broken.

5.8.2 Simulation Details

In agreement with the previously discussed shape (Sec. 5.6.2) and size studies, a [001] oriented virtual tip is built in cylinder shape with 8 nm in radius and 24 nm in height. Following the recipe for voltage protocol optimization from Sec. 5.7.2, the virtual voltage in the simulation is first increased by 10 V after a set of MD runs until 420 V, and then increased by 2 V after a set of MD runs until an evaporation event is triggered. Again, the voltage never decreases to ensure a computationally efficient data collection process. The employed interatomic potential is an embedded atom model potential from Zope and Mishin [89].

For comparison, we also performed traditional TAPSim simulations for the same tip structure. Since no MD is included in this method, an evaporation criterion is used to determine the evaporation event which is based on the magnitude of field-induced forces and empirical evaporation fields. Since the hypothesis to test is if Al or Ti should have the lower evaporation field, we use type 1 and type 2 to tag the atoms in the two layers. We set the evaporation field of type 1 to 2.6 V/Å as the high field, and that of type 2 to 1.9 V/Å as the low field. Details about the TAPSim approach and applications can be found in Refs. [41, 76].

5.8.3 Results and Discussion

Reconstruction and Surface Morphology. In this section, we undertake a comparative analysis by juxtaposing various simulation outcomes with experimental observations, focusing on the standard reconstruction outcome and the surface morphology of the tip.

As mentioned before, the reconstructed structure of [001] oriented TiAl has mixed Ti/Al planes instead of alternate Ti and Al planes in the crystal as shown in Fig. 21(a). Our simulated reconstruction result (Fig.21(b)) is consistent with the experimental observation shown in Fig. 21(c). In both cases, there is no discernible alternately layered structure.

As discussed in Sec. 5.8.1, the presence of mixed Ti/Al planes has traditionally been attributed to the preferential evaporation of one of these elements. This phenomenon can be effectively understood by considering an "evaporation pair" pattern, wherein a Ti plane and an Al plane evaporate simultaneously. Indeed, this "pair" behavior has been previously observed in field ion microscopy (FIM) studies [86, 87, 85].

As illustrated in Fig.22(a), the size of the Ti layer closely matches that of the Al layer

DISTRIBUTION A: Distribution approved for public release.

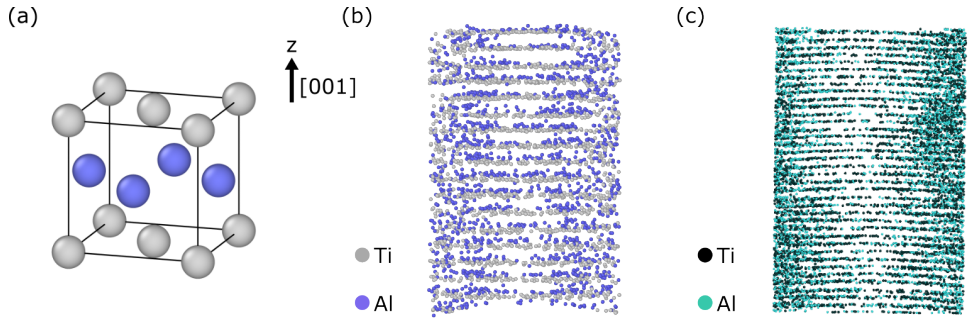

Figure 21: (a) is the structure of γ-TiAl intermetallic compound. (b) is the standard reconstruction result of simulation data from TAPSim-MD. (c) is the experimental reconstruction result of TiAl.

situated above it, whereas it is significantly smaller than the Al layer beneath. Our molecular dynamics (MD) simulation, shown in Fig.22(b), indeed replicates this "pair" pattern. Remarkably, a traditional TAPSim simulation, without the inclusion of MD, also yields the same "pair" pattern, as shown in Fig. 22(c), where the low-field cyan plane has a similar size to the high-field red plane on top of it.

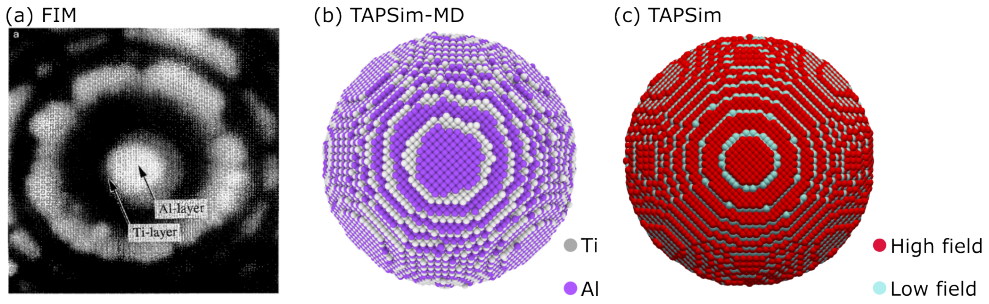

Figure 22: (a) Field-ion image of the (001) pole of a $Ti_{51}Al_{46}Cr_3$ sample, reprinted from Ref. [86]. The brighter (dimmer) contrast is Al (Ti). (b) Top view of a TiAl tip simulated by TAPSim-MD. Ti (Al) atoms are grey (violet). (c) Top view of the tip from (b), simulated by traditional TAPSim. Atoms with higher (lower) evaporation field are red (cyan).

A comparison between the simulation outcomes of TAPSim-MD and traditional TAPSim reveals that Al atoms are likely to possess a higher evaporation field, while Ti atoms are expected to exhibit a lower one. Consequently, Al atoms tend to remain on the specimen, whereas Ti atoms have a greater propensity for evaporation. This result is in agreement with most previous analyses in the literature [86, 87, 85].

Atom Trajectory and Force. As demonstrated previously, TAPSim-MD's prediction of the bilayer surface morphology along with the evaporation sequence for TiAl agree well with experimental observations without any *ad hoc* assumptions about evap-

DISTRIBUTION A: Distribution approved for public release.

oration fields or prior knowledge of charge states. The full dynamics of TAPSim-MD allows us now to study the underlying processes of the evaporation sequence from a dynamic perspective by analyzing forces and atom trajectories.

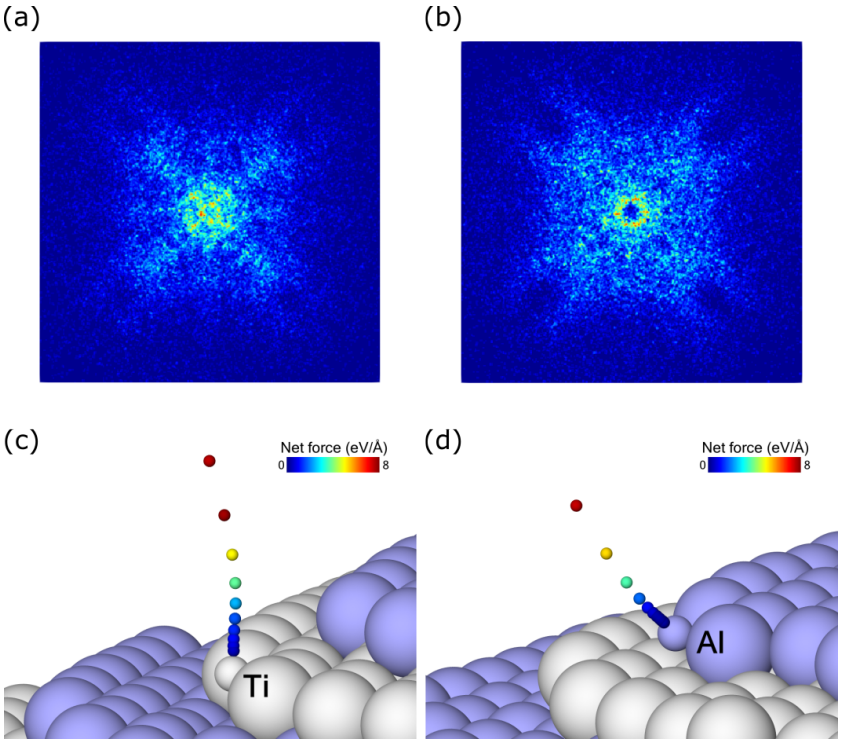

Figure 23: Field evaporation maps from TAPSim-MD simulation for (a) Ti and (b) Al atoms. The warmer the color, the higher the intensity. Further shown are examples of (c) Ti and (d) Al atom trajectories during evaporation, respectively. Ti (Al) atoms are shown in grey (violet). The equilibrium positions of the evaporating atoms are indicated by smaller balls with the same color scheme. The atom trajectories are described by a series of small dots colored by magnitudes of net forces at different instances. The warmer the color, the larger the net force.

Fig. 23 (a) and (b) depict markedly different field evaporation maps for Ti and Al: the central pole in the Ti map is more densely populated, while it is depleted in the Al map. Furthermore, the zone lines in the Ti map exhibit heightened intensity, whereas a slight depletion is observed in the Al map. These pronounced dissimilarities in the evaporation maps strongly suggest that Ti and Al follow distinctly different launch trajectories. Indeed, our observed launch trajectories for Ti and Al, as shown in Fig. 23(c) and (d), confirm this divergence: the evaporating Ti atom initially ascends vertically along the z-direction, while the evaporating Al atom departs at an angle of approximately 45° between the z-axis and the xy-plane.

Considering that the electrostatic forces should not depend on the chemical identities

DISTRIBUTION A: Distribution approved for public release.

of evaporating atoms for equal charge states but on the geometry, the distinct atom launch trajectories of Ti and Al indicate that the desorption or bond breaking processes of the two species should be distinctly different.

What adds a layer of intrigue to this observation is that, based solely on bond strength, Al would be expected to have weaker bonds than Ti. Nevertheless, it exhibits a higher evaporation field than Ti, despite Ti possessing relatively strong bonds. As mentioned, we find by means of DFT calculations along the lines of bond strengths of -0.58 eV, -0.86 eV, and -0.91 eV for Al-Al, Ti-Al and Ti-Ti bonds, respectively. While it is well-established that a comprehensive analysis of real evaporation processes should consider multiple factors, including total ionization energy and work function, our MD simulation employs induced charges to calculate electrostatic forces and otherwise solely depends on interatomic interactions. Consequently, the preferential evaporation of strongly bonded Ti atoms can be attributed to the manner in which these bonds are broken during the evaporation process.

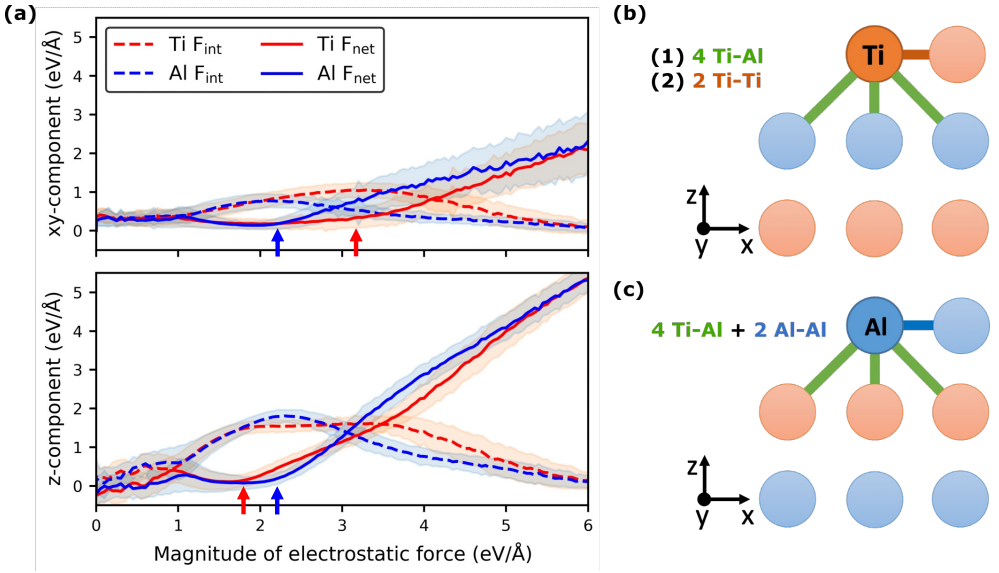

Figure 24: (a) xy- and z-components of interatomic forces (dashed lines) and net forces (solid lines) vs. the magnitude of the electrostatic force during field evaporation in TAPSim-MD simulation for an 8 nm-radius TiAl tip. Each data point is an average over 3098 Ti atoms or 2871 Al atoms. The standard deviations are indicated by shadows. The critical points are indicated by blue or red arrows for Ti or Al. The schematic bonding condition and bond breaking sequence of evaporating atoms are shown for a Ti atom (orange) in (b) and for an Al atom (blue) in (c).

In order to understand the bond breaking process, we first examine the xy- and z-components of the interatomic force and net force as functions of the electrostatic force induced by the applied voltage. As shown in fig. 24(a), when the electrostatic force induced on an atom is rather small (approximately less than 1 eV/Å), it is balanced by

DISTRIBUTION A: Distribution approved for public release.

the interatomic force, resulting in an almost zero net force in both the xy-plane and the z-direction, which makes the atom vibrate around its equilibrium position. However, as the electrostatic force increases, it begins to overcome the interatomic force and consequently gives rise to a continuously growing instead of oscillating net force, where the atom starts to evaporate. With regard to Al (blue lines), the continuous growth of the net force (solid lines) in both xy-plane (upper panel) and z-direction (lower panel) start when the electrostatic force is about 2.2 eV/Å, as indicated by blue arrows. As for Ti atoms (red lines), the continuous growth of the lateral net force starts around an electrostatic force of 3.2 eV/Å, while the growth of the z-component starts around an electrostatic force of 1.8 eV/Å, as indicated by red arrows. The simultaneous growth of the lateral and z-components of the net force of Al suggests that bond breaking in the xy-plane (2 Al-Al bonds) and z-direction (4 Ti-Al bonds) should occur around the same time. In contrast, for Ti, the in-plane and the out-of-plane bond breaking start at distinctly different times, first in the z-direction (breaking 4 Ti-Al bonds at an electrostatic force of $\sim$ 1.8 eV/Å), and second in the lateral direction (breaking 2 Ti-Ti bonds at an electrostatic force of $\sim$ 3.2 eV/Å). Schematic plots of the bond breaking processes for the two species along these findings are shown in Fig. 24(b)-(c).

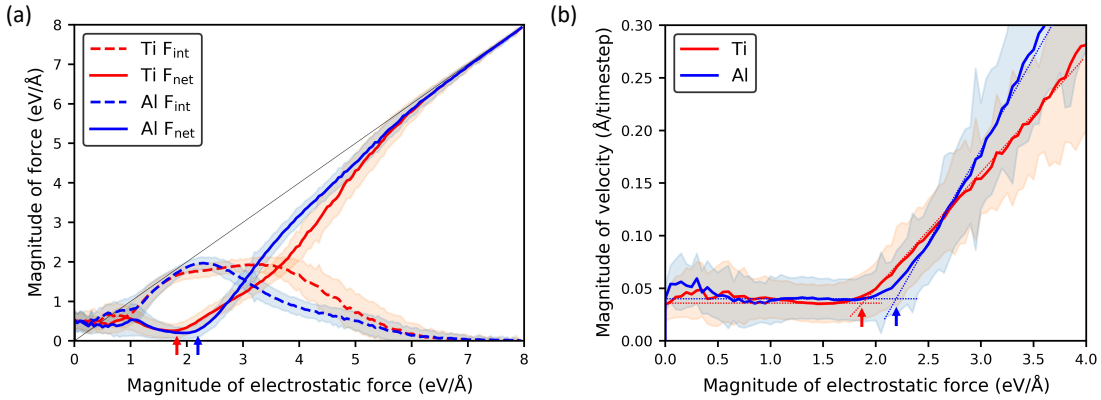

Figure 25: (a) Magnitude of interatomic and net force vs magnitude of electrostatic force. The thin black solid line indicates y=x. (b) Magnitude of velocity vs magnitude of electrostatic force. Each data point is averaged over 3098 Ti atoms and 2871 Al atoms. The standard deviations are indicated by shadows. The critical points are indicated by blue or red arrows for Ti or Al.

In order to show why the two-step bond-breaking process of Ti results in its preferential evaporation, we examine the magnitude of both the total net force and the resulting velocity as functions of the electrostatic force. Figure 25(a) clearly shows that the net force acting on the Ti atom (red line) doesn't exhibit continuous growth until the electrostatic force surpasses approximately 1.8 eV/Å, indicated by a red arrow, while this point is reached later for Al (blue line), at around 2.2 eV/Å, indicated by a blue arrow. Consequently, when subjected to the same magnitude of electrostatic forces, it becomes easier to initiate the evaporation of a Ti atom. Along with that, the two-step

DISTRIBUTION A: Distribution approved for public release.

bond-breaking process of Ti is also reflected on the growth of the interatomic force (red dashed line), where two local maxima can be found at around 1.9 eV/Å and 3.3 eV/Å electrostatic force, corresponding to the first and second bond-breaking events of Ti respectively. In contrast, there is only one interatomic force maximum of Al (blue dashed line) at around 2.3 eV/Å electrostatic force, which is associated with the one-step bond-breaking process of Al. As a side note, the electrostatic force and internal force can not completely offset each other after the atom leaves its equilibrium position as a result of the different anisotropic features of the interatomic force and electrostatic force as discussed in Sec. 5.7, which explains why the growth of the interatomic force deviates from the line of $y = x$ at the initial stage of evaporation.

The conclusion of preferential evaporation of Ti can also be drawn from analyzing the velocities shown in Fig. 25(b). For both Al and Ti, the atoms exhibit vibrational motion around their equilibrium positions with nearly zero velocity before the electrostatic force starts to dominate over the interatomic force. As the electrostatic force intensifies, a critical point is reached at approximately 1.8 eV/Å for Ti and 2.2 eV/Å for Al, quantified by the electrostatic force at the intersection of the linear-acceleration range with the constant, low-velocity range. At this point, the interatomic force cannot balance the electrostatic force anymore, and the velocity starts to linearly grow with the increasing electrostatic force. Once again, when considering the application of an equivalent magnitude of electrostatic forces, we find that the evaporation of a Ti atom is easier than that of Al, equivalent to a lower evaporation field of Ti compared to Al. Interestingly, the velocity analysis and especially the determined intersection point suggests that it is only the first bond-breaking event in Ti that seems to correlate with the effective evaporation field rather than the second one.

In summary, we have revisited the disrupted evaporation sequence in [001]-oriented γ-TiAl, a phenomenon that often leads to erroneous results in reconstruction due to the different evaporation fields exhibited by different species. Employing our full-dynamics approach, we provide an *ab initio* confirmation that Ti requires a lower electrostatic force along with a lower evaporation field to evaporate, a finding that aligns well with the majority of experimental observations documented in the literature.

More importantly, through a comprehensive examination of atom trajectories and forces, we have unveiled a step-wise bond-breaking process for Ti, in contrast to the simultaneous bond-breaking process observed for Al. This discovery offers a compelling explanation for the seemingly counterintuitive preferential evaporation of the strongly bonded Ti atoms.

5.9 Orientation Bias in APT Reconstruction: GP Zones in Al-Cu Alloys

5.9.1 Background

Precipitation hardening or age hardening is an important heat treatment technique to enhance the strength and hardness and optimize the mechanical performance of an alloy. This process has been extensively studied in Al-Cu alloys as a prototypical system for age-hardening alloys. Starting from a supersaturated solid solution, Guinier–Preston

DISTRIBUTION A: Distribution approved for public release.

(GP) zones form in the early stages of the aging process, where they go through "GP-I" and "GP-II" stages to eventually form the metastable but primary strengthening θ' phase, which eventually evolves into the stable θ phase. GP-I zones are comprised of monolayer Cu platelets on {100} planes of the face-centred cubic (FCC) Al–Cu solid solution matrix. It is believed that GP-II zones are formed by two or more Cu {200} monolayer platelets separated by three Al {200} planes. The metastable θ' phase is coherent with the lattice of the solid solution matrix and has a distorted fluorite (C1) structure with body-centered tetragonal Bravais lattice and the stoichiometry Al_2Cu. The final stable phase θ is an incoherent phase with the same stoichiometry Al_2Cu and has a tetragonal C16 structure.

Characterization of GP zones is challenging due to the single-Cu-layer platelet structures, which require atomic resolution. APT is a powerful 3D technique capable of resolving both the atomic structure and the chemical composition of a material, and is therefore widely used to visualize microstructural features such as precipitates. However, as we have shown previously, artifacts can occur during field evaporation and be further introduced by the reconstruction algorithm, resulting in unrealistic reconstruction results as what we have seen in the case of TiAl in Sec. 5.8. For small precipitates (on the scale of a few nm), it has been reported that there is a shift of the relative positioning of matrix and precipitate atoms of GP zones in Al-Ag and Al-Mg-Sc alloys due to the difference in evaporation field between the matrix atoms and atoms constituting the precipitates [90]. In that work, these so-called "chromatic aberrations" were identified in the plane of evaporation, but not otherwise, raising questions about any artifacts in depth along the sample axis. Furthermore, in APT experiments such as Ref. [91], it is not clear if the resolution is good enough to discern the Cu monolayer structures of GP zones in Al-Cu alloys.

Here, we will examine in the case of the GP-I zone the orientation biased reconstruction artifacts brought about by the anisotropy of the precipitate platelets and explore if the resolution limit of APT should be good enough to discern the Cu monolayer. We will show that the stronger bonds of Cu atoms cause preferential retention of GP zones on the surface, similar to what was found for dissolved Cu in Au [47]. Assumptions about the spherical tip shape and the simple projection law in the standard reconstruction algorithm give rise to artifacts that are biased by the orientation of platelets, i.e., parallel to the sample axis or perpendicular to the sample axis. By performing TAPSim-MD simulations, we will identify the origin of different reconstruction artifacts observed in platelets placed in different orientations.

5.9.2 Experimental and Simulation Details

An Al-4 wt.%Cu (Al-1.74 at.%Cu) ingot was prepared from high-purity Al (99.99%) and Cu (99.9%) bulk metals with an Edmund Bühler GmbH arc melter. The ingot was cold rolled and heat treated at 550°C for 2 h and 160°C for 1 h in a quartz tube back-filled with Ar, followed by water quenching. The heat treatment should produce a predominate GP-I phase in this alloy according to Ref. [92]. A sectioned surface was ground and polished down to 1 μm surface finish for scanning electron microscopy

DISTRIBUTION A: Distribution approved for public release.

(SEM) observation and electron backscatter diffraction. Samples for APT were prepared using a standard lift-out with a Thermo Fisher Helios 650 Nanolab SEM/focused ion beam from a ⟨001⟩-orientated grain identified by electron back scattered diffraction. The sharpening process was performed with a Thermo Fisher Helios G4 plasma FIB UXe. APT experiments were conducted using a Cameca LEAP 5000XR instrument in voltage mode with a base sample temperature of 30 K, a detection rate of 1%, a pulse fraction of 20%, and a pulse frequency of 250 kHz. Data reconstruction was conducted using the Cameca AP suite software 6.3. The value of image compression factor was estimated as 1.59 according to the best fitting results of the evaporation map indexed by APS-integrated Orientation Imaging Microscopy. The field factor was optimized as 6.4 to create a (002) plane spacing close to 0.2 nm. The measured composition was Al-1.83 at.%Cu, close to the targeted nominal composition.

The simulations were carried out using the full-dynamics field evaporation simulation code TAPSim-MD [53]. Virtual tips are built in cylinder shapes with two sizes: 6 nm in radius and 18 nm in height or 8 nm in radius and 24 nm in height. Considering the computational performance for this material, smaller tips are used as long as stable results are produced; otherwise, larger tips will be used. For modeling of GP zones, monolayer Cu platelets in the shape of circular disks are created in the FCC Al matrix by substituting Al atoms with Cu atoms. The lattice constant of the Al matrix is 4.05 Å, which is the experimental value as well as the relaxed value the interatomic potential used. The sizes of the Cu platelets are 2-4 nm in diameter. Following the previously described optimization of the voltage protocol for 6 nm tips, we begin by increasing the virtual voltage by 10 V after a set of MD runs until it reaches 120 V. Subsequently, we transition to a smaller increment of 1 V after a set of MD runs, continuing in this manner until an evaporation event is initiated. When no further evaporation happens, another 1V increment follows, and this process is iterated until the end of the simulation. The same is done for the 8 nm-radius tip in initial steps of 10 V until 250 V is reached, followed by 5 V increases. The employed interatomic potential is an angular-dependent interatomic potential (ADP) from Apostol and Mishin [93]. ADP is a generalization of an embedded atom model (EAM) potential with angular terms to represent angular-dependent forces [94, 95]. This potential has been well tested for atomistic simulation of precipitation hardening of Al-Cu alloys by the authors. We have also tested an EAM potential [96] as a faster alternative, but found that only ADP is able to model a stable θ' phase, and therefore found it more suitable for the present simulations.

5.9.3 Results and Discussion

In this section, precipitate platelets parallel to the sample axis are referred to as vertical, whereas platelets perpendicular to the sample axis are referred to as horizontal. The sample axis, which is also the z-axis, is along the [001] direction.

Vertical Precipitates. Figure 26(a) displays the distribution of Cu atoms within the reconstructed structure obtained from experiments within our collaboration. Notably, the perceived thickness of Cu-enriched regions appears to be generally greater in vertical

DISTRIBUTION A: Distribution approved for public release.

platelets compared to horizontal ones. Consequently, when comparing precipitates in both orientations collectively, the absolute thickness of the reconstructed precipitates lacks meaningful discriminatory value.

As an illustration, consider the vertical precipitate presented in Fig. 27(a). The thickness of this platelet measures approximately 3.5 nm, equivalent to about 17 (002) lattice planes, as determined by the extent of Cu enrichment in its distribution. In this case, we cannot identify any monolayer Cu, as the platelet thickness significantly exceeds that of the expected GP-I zone or even a typical GP-II precipitate, which means it is inherently unreliable to determine, solely from the reconstructed thickness, which GP zone phase a Cu-enriched platelet belongs to. This holds particularly true when no prior knowledge is available regarding the phases present in the sample alloy.

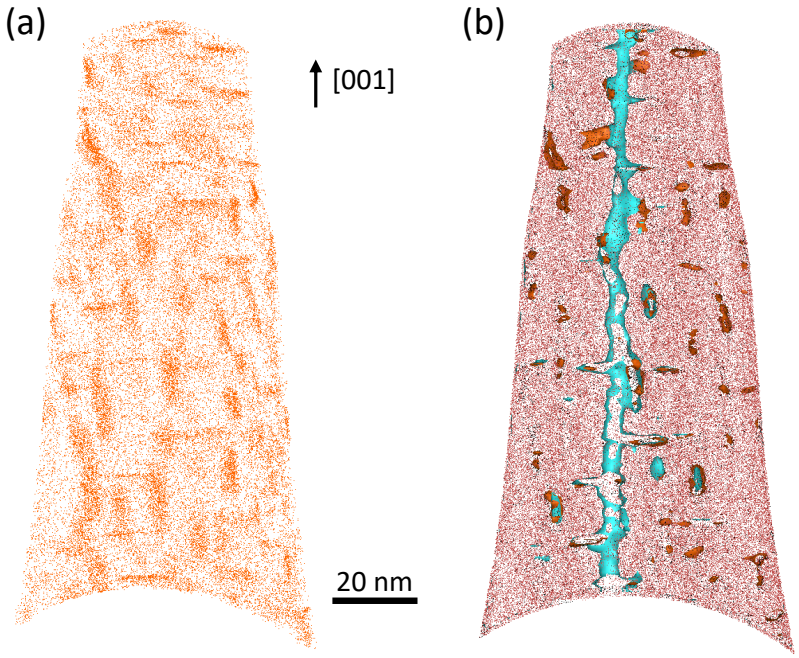

Figure 26: (a) Cu atoms in a 10 nm-thick slice of the reconstructed structure as measured by LEAP. (b) A 10 nm-thick slice of the reconstructed structure through the primary pole, where Al and Cu atoms are shown by red and black dots respectively, with cyan isosurface at an Al density of 20 nm^{-3} and orange isosurface at a Cu density of 1.5 nm^{-3}.

Similar conclusions are drawn from simulation results, where of course the simulations have the advantage of precisely knowing the phase and size of the simulated precipitate. Figure 28(c) and (d) provide front and side views, respectively, of a reconstructed 2 nm-radius GP-I zone within a 6 nm-radius virtual tip in the simulation.

As depicted in Fig. 28(c), the reconstructed Cu platelet exhibits a slight lateral distortion within the plane, indicated by its oval shape with a shorter axis along the [001]

DISTRIBUTION A: Distribution approved for public release.

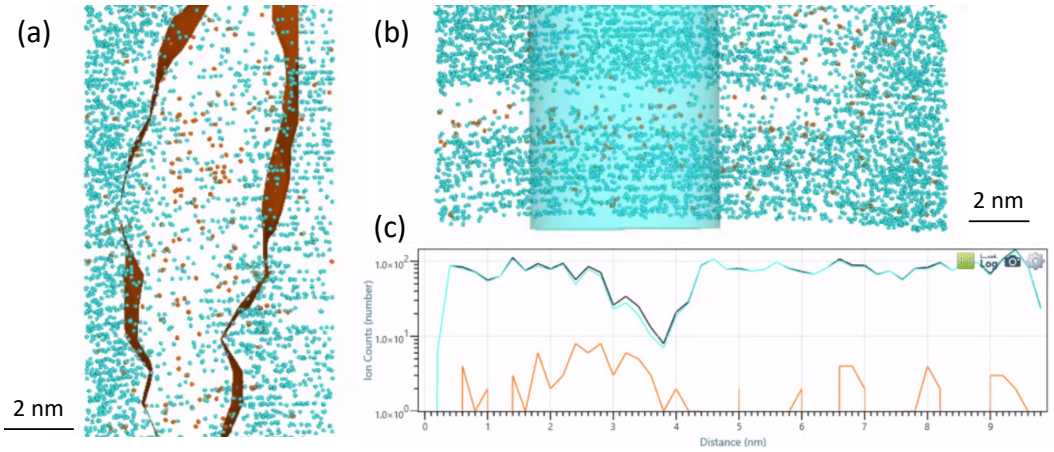

Figure 27: Experimental examples of (a) vertical and (b) horizontal precipitates. The slices are 1.5 nm thick. (c) 1D density profile along the cylindrical volume shown in (b) from the bottom to the top. Al and Cu atoms are colored cyan and orange, respectively.

direction, measuring approximately 4 nm. Nonetheless, the overall shape and size of the reconstructed platelet closely resemble the original one in Fig. 28(a).

This is however different for the "thickness" direction, where the distribution of Cu atoms is very diffusive as shown in Fig. 28(d). The reconstructed thickness extends to approximately 3 nm, equivalent to 15 (002) lattice planes, a dimension far exceeding that of the original Cu monolayer in Fig. 28(b) or even a typical GP-II precipitate, consistent with what we see in the experiment.

To investigate the origin of this spread of Cu, we also performed a simulation in an elemental Al tip with the same size for comparison. The Al atoms located in the same region of the platelet in Fig. 28(a) are marked, and the reconstructed positions of these marked Al atoms in deep blue are shown in Fig. 28(e) and (f). These marked Al atoms have a very similar distribution compared to the Cu atoms in Fig. 28(c) and (d). Therefore, the spread of Cu, especially in thickness, is inevitable considering the intrinsic randomness brought about by the field evaporation process.

Summarizing these results, we find that the reconstruction of vertical Cu platelets exhibits satisfactory fidelity regarding the shape and the size, but displays significant variability in terms of thickness. The original Cu monolayer structure is entirely lost during the reconstruction process. The considerable spread of Cu in the thickness dimension renders it impractical to reliably distinguish between GP-I and GP-II phases.

Horizontal Precipitates. Figure 26(b) represents a cross-sectional view of the reconstructed structure, taken through the primary pole, as obtained from experimental data. The sample axis aligns with the [001] direction. The cyan isosurface contour depicting Al marks the location of the primary pole (in this case, the (002) pole) and reveals the presence of horizontal GP zones surrounding the pole. Notably, there is a conspicuous absence of Al above the Cu-enriched regions within these zones, as evident

DISTRIBUTION A: Distribution approved for public release.

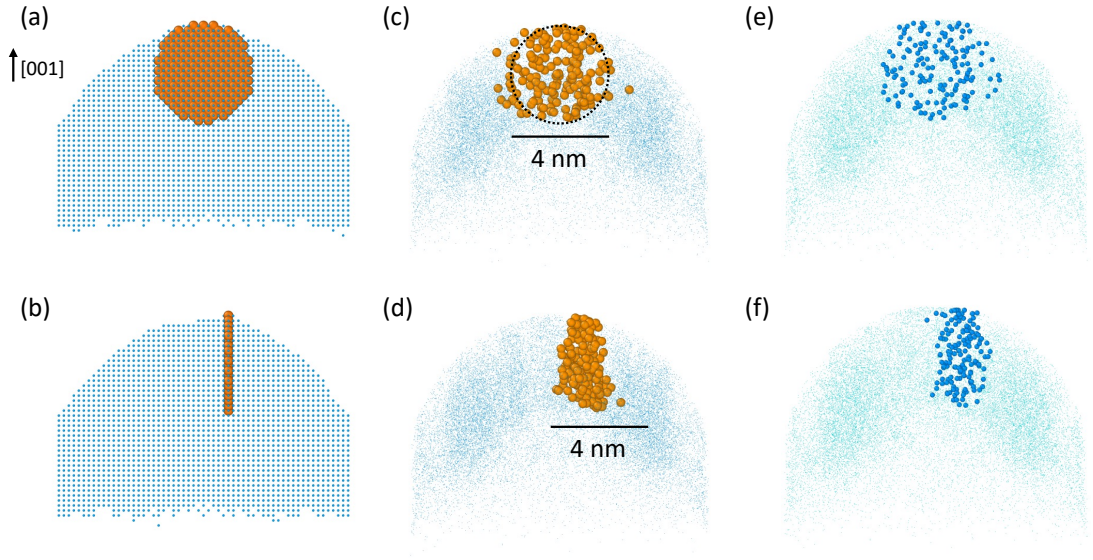

Figure 28: (a) and (b) are front and side views of the original structure of the simulated vertial GP-I platelet with a 2 nm radius in a 6 nm-radius tip. (c) and (d) are front and side views of the reconstructed GP-I platelet. The dashed circle is 4 nm in diameter as comparison to the size of the reconstructed platelet. Cu (Al) atoms are colored orange (grey). (e) and (f) are front and side views of the reconstructed elemental Al tip with atoms in the same region of the platelet in (a) marked and colored deep blue.

in the zoomed-in example shown in Fig. 27(b).

In Fig. 27(c), a 1D density profile is plotted along the cylinder marked in Fig. 27(b) that traverses the region of interest, extending from the bottom to the top. This profile indicates that the Cu density is relatively high within the range of 1.5 to 3.5 nm along the x-axis, while the Al density remains relatively low within the span of 2.5 to 4.5 nm. The thickness of this horizontal platelet measures approximately 1.5 nm, equivalent to about 7 (002) lattice planes. While it is 50% thinner than the vertical platelet in Fig. 27(a), it still significantly exceeds the dimensions of both GP-I and GP-II zones.

It is worth noting that the artifact involving the shift of the Cu-enriched region and the Al-depleted region is reminiscent of the "chromatic error" reported in Ref. [90], albeit in the present case, the shift occurs in the thickness direction and is specific to horizontal platelets. In contrast, there is no discernible shift in vertical precipitates. Similar artifacts in horizontal GP zones were previously reported by Bigot et al. [97], where they also observed the shift in Al depletion and Cu enrichment. Additionally, they noted an apparent Al enrichment preceding the Al depletion, a feature that is not apparent in our results.

The shift in Al depletion and Cu enrichment arises from the vastly different evaporation fields exhibited by the Al matrix and Cu precipitates. Due to the stronger bonds of

DISTRIBUTION A: Distribution approved for public release.

Cu atoms, they are less inclined to evaporate, disrupting the evaporation sequence [47]. However, the standard reconstruction algorithm still operates under the assumption of an ideal evaporation sequence, resulting in the artificial depletion region [98].

In addition to the observed shift in Al depletion and Cu enrichment within reconstructed GP zones, another noteworthy observation is the infrequency of well-aligned horizontal monolayers of Cu after reconstruction. Instead, the distribution of Cu atoms appears highly dispersed. This result is somewhat puzzling, given the expectation of the usually rather controlled evaporation behavior of atoms in (002) lattice planes. In these planes, a regular evaporation sequence of edge atoms from each terrace typically leads to a rather accurate reconstruction along the sample axis around the center pole. This is evidenced by the well-aligned Al matrix atoms, which exhibit distinct (002) atomic layers in Fig. 27.

Bigot et al. reported a similar abnormal thickness spread for horizontal Cu platelets [97]. They attributed this spread of Cu in thickness to the local magnification effect resulting from the preferential retention of Cu. However, quantifying the impact of local magnification in experimental data is challenging, primarily because the presence of Cu solutes in the matrix can significantly influence the determination of Cu density within the reconstructed precipitate. As Cu atoms within the precipitates become dispersed during reconstruction, they become indistinguishable from the Cu solute atoms. This makes it difficult or even impossible to perform a data-driven quantification of local magnification from experiment, which is a task we aim to address in the following by simulation.

To shed light on this issue, TAPSim-MD simulations were conducted for horizontal Cu platelets. Figure 29 shows the evaporation of two horizontal Cu monolayers from an 8 nm-radius tip, one with a 2 nm diameter and the other with a 3 nm diameter, respectively. In these simulations, the 2 nm Cu platelet was deliberately placed off the sample axis, while the 3 nm Cu platelet was centered. These two Cu platelets were separated by a distance of 10 Al-layers and underwent consecutive evaporation. We found that both Cu platelets exhibit a significant reluctance to evaporate when compared to the neighboring Al atoms in the matrix. This reluctance results in the formation of large local curvatures around the Cu platelets, as expected. When the electric field reaches a sufficiently high level, all Cu atoms within the platelets are rapidly evaporated in unison.

In simulation, even if clusters of atoms undergo evaporation, the detection rate still remains nearly 100%, as each individual virtual atom is traceable, except for a few outliers excluded by the program for numerical reasons. The standard reconstruction result is shown in Fig.30(a) and (b) for 2 nm and 6 nm slices, respectively. In the 2 nm slice, (002) lattice planes with a 0.2 nm interplanar distance are clearly visible, accompanied by a distinct region depleted of Al above the reconstructed Cu layer, consistent with experimental observations.

An intriguing observation is a layer of Al atoms within the Al-depleted region, indicated by the red arrow, which aligns with a similar finding in the experimental result shown in Fig.30(c) with a red arrow. By tracing these Al atoms in the layer back to their original positions, they are identified as belonging to the second Al layer above the Cu monolayer, shown in cyan and marked with a red arrow in Fig.30(d). Conversely,

DISTRIBUTION A: Distribution approved for public release.

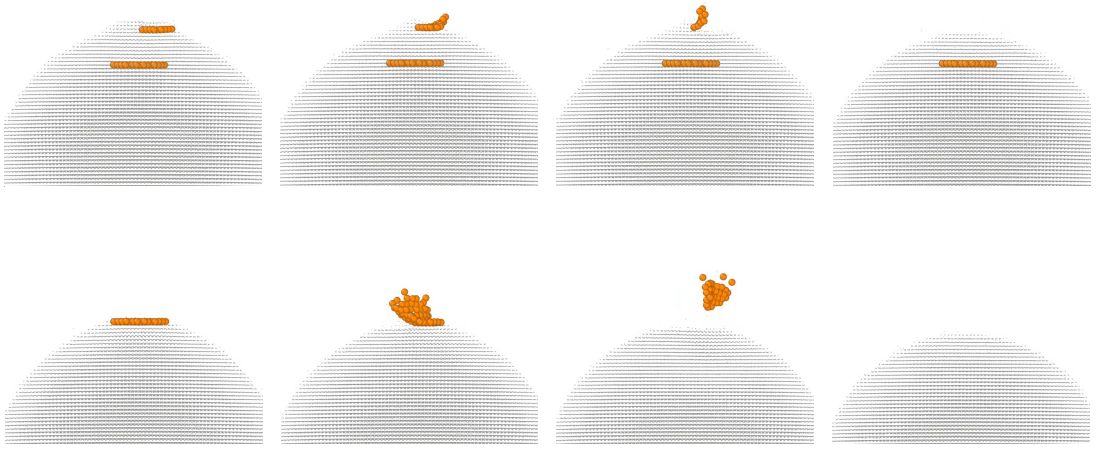

Figure 29: Simulation of the evaporation process in an 8 nm-radius virtual tip containing two horizontal GP-I zones, one with a diameter of 2 nm and the other with a diameter of 3 nm. Al atoms are represented in grey, while Cu atoms are depicted in orange.

the first Al layer above the Cu monolayer, marked with a black arrow in Fig.30(d), evaporates simultaneously with the Cu monolayer beneath it, as shown in Fig.30(e). This zoomed-in snapshot reveals the evaporation of the 3 nm-diameter platelet in the simulation, with a black arrow indicating the Al layer above the Cu monolayer. The standard reconstruction algorithm combines the co-evaporated Al and Cu layers into the same reconstructed layer, analogous to the "mixed layer" reconstruction artifact observed in TiAl, as discussed in Sec.5.8. Consequently, the first Al layer reconstructed above the Cu platelet corresponds to the second Al layer above the Cu monolayer in the original structure.

The strong Al-Cu bonding between the Cu monolayer and the adjacent Al layer makes the first Al layer above resistant to evaporation. As for the reason why this Al layer with weaker lateral Al-Al bonds does not evaporate independently but rather together with the Cu monolayer beneath it, it may be explained by the mechanism proposed in Sec.5.8 for TiAl, where alternate Ti/Al layers are present. In [001] orientated TiAl, Al atoms are harder to evaporate even though the Al-Al bond is much weaker than the Ti-Ti bond, leading to the simultaneous evaporation of the Ti layer beneath along with the top Al layer. Fig. 30(e) also shows that the Al layer beneath the Cu monolayer becomes highly unstable after the Cu monolayer starts to detach. These Al atoms quickly evaporate in response to the detachment process of the Cu monolayer, owing to the weak interlayer connections between Al layers.

Due to the assumptions adopted in the standard reconstruction approach, lattice planes appear bent downward in regions away from the sample axis. This artifact is very pronounced in the simulation results depicted in Fig.30(a), primarily due to the

DISTRIBUTION A: Distribution approved for public release.

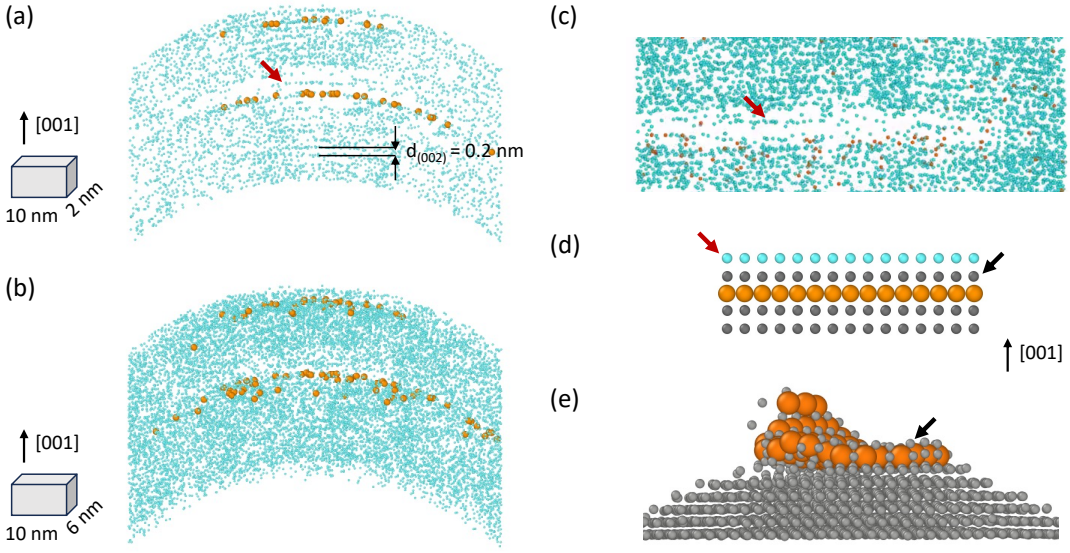

Figure 30: (a) and (b) represent 2 nm-thick and 6 nm-thick slices, cut parallel to the z-axis respectively, of the reconstructed structure from the simulation shown in Fig. 29. (c) corresponds to the same experimental result as shown in Fig. 27(b). (d) displays a section of the original virtual tip. (e) captures a snapshot of the evaporation process of the 3 nm-diameter platelet within the 8 nm-radius tip. Cu atoms are colored in orange, while Al atoms are depicted in cyan or grey.

small size of the virtual tip. However, this bending is also visible in the experimental results shown in Fig.30(c), where lattice planes near the right edge of the figure exhibit a downward bend. Besides the bending effect, the reconstructed Cu-enriched platelets in simulation disperses over a wide range in size. The projection of the reconstructed 2 nm-diameter Cu platelet spans about 4 nm in diameter, while the 3 nm-diameter Cu platelet projects to around 9 nm in diameter.

Regarding thickness, the simulation reveals only monolayers of Cu, without any noticeable spread, which differs from experimental and literature results where the observed considerable spread was attributed to the local-magnification effect [97]. Since the platelet is more or less bent after reconstruction, the 1D profile of the region of interest obtained through thin flat slices may not accurately represent its true thickness. Especially when the analyzed slice isn't sufficiently thin, such as in Fig.30(b), where a 6 nm-thick slice is presented for comparison, a broader distribution of Cu appears around the center when examining its 2D projection from the front view. However, even in this case, the Cu distribution in thickness is only approximately 0.5 nm, significantly smaller than the Cu-enriched range seen in the experimental result displayed in Fig.27(c), which spans about 1.5 nm. Considering the much larger size of the actual tip in the experiment which results in a far smaller curvature around the central pole, the bending effect on

DISTRIBUTION A: Distribution approved for public release.

the reconstructed platelet should exert even less influence on the Cu density analysis in the region of interest. Therefore, it should not be the reason for the observed spread of Cu in thickness.

Another factor that may influence the reconstruction quality in experiments is evaporation of clusters of atoms, for example, the clusters we see in the simulation in Fig. 29. Evaporation of clusters or molecules is often observed in non-metal samples, such as oxides, and can lead to a significant loss of spatial resolution [80]. Because clusters of atoms may dissociate and change trajectories during their flight to the detector, and real detectors do not detect large numbers of atoms that arrive simultaneously, experiments are usually performed and controlled very carefully to evaporate one atom at a time. However, even under controlled conditions, cluster evaporation events can still occur. Thus, if the clusters observed in our simulation were to manifest as smaller entities in the actual experiment, they may be able to explain the spread of Cu atoms in thickness of reconstructed horizontal Cu platelets. To verify this hypothesis, a thorough examination of the raw mass spectrometry data is necessary to determine whether such clusters of atoms are present in the experimental results. For a meaningful comparison, a more quantitative analysis of the simulation data, such as a statistical investigation into the size distribution of atom clusters, would also be needed.

Summarizing this section, the use of the full dynamics field evaporation tool TAPSim-MD has allowed us to reproduce and elucidate orientation-dependent artifacts in the APT reconstruction of GP zones in Al-Cu alloys. We show that the reconstructed APT data fail to discern the Cu monolayer structures of GP zones, whether they are oriented horizontally or vertically. Consequently, APT cannot reliably identify the exact phases of GP-I or GP-II.

We also show that there is a lateral spread of Cu atom in reconstructed (002) lattice planes arising from the intrinsic randomness of field evaporation. This, in turn, results in artificially increased thickness in the case of vertical Cu platelets. While the reconstructed thickness of horizontal Cu platelets is smaller than that of the vertical ones, we have uncovered additional reconstruction anomalies for this case. These anomalies include the displacement of Al depletion and Cu enrichment, the simultaneous evaporation of the Cu monolayer and the Al layer above it, and an unexpected dispersion of Cu atoms in the thickness direction. We have successfully explained the first two artifacts, attributing them to the distinct evaporation fields of GP zones and the Al matrix, as well as the anisotropic bonding characteristics within the Al-Cu-Al structure. However, further investigations are required to conclusively determine the origin of the last artifact.

5.10 Machine-Learning Based Reconstruction

As a final step, we investigated if our forward-modeled data can be used to train improved reconstruction through machine learning. For that, we trained a supervised neural network with forward modeled data from the GP-zone simulations from Sec. 5.9. The input data consisted of the detector signal, i.e., the x, y coordinate on the detector, time of arrival, and element, which are the data measured in an actual experiment. The

DISTRIBUTION A: Distribution approved for public release.

output data to predict is the original position of the atom, which we accurately know in simulation and thus can minimize the deviation between predicted and original position in the training of the machine learning model. Due to the large number of atoms evaporated, deep neural networks can be used which can be trained to be highly accurate. Once the model is trained for a given material system, it then can be used to perform reconstruction on actual experimental data.

To demonsrate the achievable improvement, we have taken the TAPSim-MD forward data from Sec. 5.9 to train a neural network, and then compared the machine-learning based reconstruction with traditional reconstruction. Figure 31 shows the results. While standard reconstruction widens the evaporated single-atom thick GP-I zone into a magnified non-spherical disk with magnified radius and a thickness of at least 2 nm, the neural network shows significant improvement in uncertainty with a roughly 2-atom wide uncertainty in disk thickness and an only slightly increased disk radius. Thus, with machine learning based reconstruction trained based on hi-fidelity forward modeled data, the longstanding promise of APT as an atomic-resolution 3D technique, which previously it never was, can finally become a reality, which will constitute a giant leap for the LEAP field.

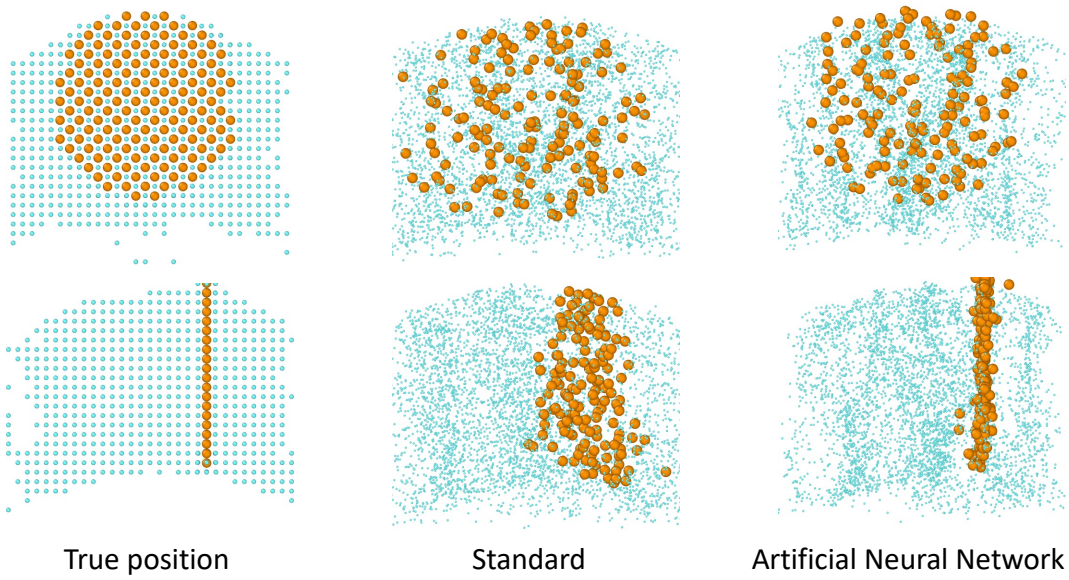

Figure 31: Cu-GP zone in Al. Left: original virtual sample, middle: structure from standard reconstruction after field evaporation, right: machine-learning based reconstruction using an artifical neural network. Top row is front view, bottom side view.

DISTRIBUTION A: Distribution approved for public release.

5.11 Summary

In this project multidisciplinary approaches to investigate material properties concerning the atomic behavior in field evaporation in atom probe tomography were developed to assess reconstruction fidelity, uncertainty, and artifacts in APT reconstruction. The project also had the goal of improving the quantitative capability of the APT technique. We developed the full-dynamics field evaporation simulation approach TAPSim-MD, which combines classical electrostatics with molecular dynamics to overcome the limitations of previous harmonic-transition-state-theory (TST) based models in describing field evaporation. Without *ad-hoc* assumptions about evaporation fields and launch velocities, field evaporation is integrated as part of molecular dynamics simulation in TAPSim-MD, which allows full access to the dynamic behavior of each single atom during field evaporation. We examined the reliability of our approach in terms of the electric field and forces. The electric field solution was validated by showing reasonable agreement to electron holography measurements. The use of superposition of induced electrostatic and interatomic forces as a reasonable approximation of the total force was demonstrated by checking consistency with DFT calculations. We also discussed the influence of interatomic potentials on simulation results, as the simulation can only be as realistic as the chosen interatomic potential.

We then demonstrated the power of this approach by applying it to different metallic materials. We discussed the basic properties of virtual emitters observed in simulations including steady-state tip shapes and associated critical voltages. Along with the critical voltages, we obtained critical evaporation fields derived in a variety of elemental materials to be directly related to the tabulated zero-barrier evaporation field data in the literature. Both simulated critical voltages and critical evaporation fields have excellent correlation to the tabulated values. In addition, an average sublimation energy of an high entropy alloy (HEA) was also derived for examination of alloying effects, where we found a "mixed" critical voltage resulting from the homogenization of bonds in the HEA.

To further validate the power and usefulness of this approach, we presented three case studies involving elemental metals, an intermetallic compound, and precipitates in an alloy. These case studies have led to new physical and data-driven explanations of artifacts and aexperimental observations. The first case study focused on simulating and explaining enhanced zone lines in field evaporation maps which were found to be dynamic features and are thus outside of the reach of TST-based models. The TAPSim-MD approach naturally reproduces enhaned zone lines and allowed us for the first time to answer the long-standing question about their origin. We showed for the canonical example of a $\langle 110 \rangle$ oriented tungsten tip that the magnitudes of interatomic forces and field-induced forces are comparable during the evaporation process. However, small misalignment of the two forces can deviate the trajectory of evaporating atoms from their local field directions, leading to accumulation of detector hit events around certain zone lines and thus enhances them.

The second case study introduced a new mechanism proposed from a dynamic perspective to explain the simultaneous evaporation of adjacent Ti and Al layers in [001]-oriented γ-TiAl which leads to the "mixed" layer artifact seen in standard reconstruction. By uti-

DISTRIBUTION A: Distribution approved for public release.

lizing our full-dynamics approach, we provided an *ab initio* confirmation that Ti requires a lower electrostatic force along with a lower evaporation field to evaporate. These findings align well with the majority of experimental observations reported in the literature. More importantly, through a comprehensive examination of atom trajectories and forces, we have unveiled a step-wise bond-breaking process for Ti, which is in contrast to the simultaneous bond-breaking process observed for Al. This discovery offers a compelling explanation for the seemingly counterintuitive preferential evaporation of the strongly bonded Ti atoms.

The last case study was concerned with the inherent inaccuracies of standard APT reconstruction when it comes to resolving monolayer structures of Guinier–Preston (GP) zones in Al-Cu alloys. Utilizing our full-dynamics simulation tool, we successfully reproduced and elucidated orientation-dependent artifacts in the standard APT reconstruction of GP zones in Al-Cu alloys. Based on both simulation and experimental results, we showed that reconstructed APT data are incapable of distinguishing the monolayer structures of GP zones, whether they are oriented horizontally or vertically to the sample axis. Consequently, APT cannot reliably identify the exact phases of GP-I or GP-II. Additionally, the intrinsic randomness brought about by field evaporation results in artificially increased thickness in the case of vertical Cu platelets. Our investigation also uncovered additional reconstruction anomalies for horizontal Cu platelets. These anomalies included a displacement between Al depletion and Cu enrichment, which were caused by the distinct evaporation fields of GP zones and the Al matrix. Furthermore, simultaneous evaporation of the Cu monolayer and the Al layer above it was observed, a phenomenon brought about by the anisotropic bonding characteristics within the Al-Cu-Al structure. Lastly, an unexpected dispersion of Cu atoms in the thickness direction was noted in experimental results. Further investigations are required to conclusively determine the origin of this phenomenon.

Finally, we have shown that the data produced with our new forward simulation method can be used as input to train machine learning models that can reconstruct experimental data with vastly decreased uncertainty and can finally achieve the atomic resolution that APT has promised its users for all these years without delivering it.

5.12 Acknowledgements

The award for this project, No. FA9550-19-1-0378, has been directed by AFOSR PM Dr. Ali Sayir). Computing resources were supplied and maintained by the Ohio Supercomputer Center [99] under grant number PAS0072.

References

[1] M. K. Miller and R. G. Forbes, *Introduction to Atom-Probe Tomography*, pp. 1–49. Boston, MA: Springer US, 2014.

[2] T. F. Kelly, P. P. Camus, D. J. Larson, L. M. Holzman, and S. S. Bajikar, "On the

DISTRIBUTION A: Distribution approved for public release.

many advantages of local-electrode atom probes," *Ultramicroscopy*, vol. 62, no. 1, pp. 29–42, 1996.

[3] Vurpillot, Bostel, and Blavette, "The shape of field emitters and the ion trajectories in three-dimensional atom probes," *Journal of Microscopy*, vol. 196, 1999.

[4] P. Bas, A. Bostel, B. Deconihout, and D. Blavette, "A general protocol for the reconstruction of 3d atom probe data," *Applied Surface Science*, vol. 87-88, pp. 298–304, 1995.

[5] E. A. Marquis, B. P. Geiser, T. J. Prosa, and D. J. Larson, "Evolution of tip shape during field evaporation of complex multilayer structures," *Journal of Microscopy*, vol. 241, no. 3, pp. 225–233, 2011.

[6] F. De Geuser, W. Lefebvre, F. Danoix, F. Vurpillot, B. Forbord, and D. Blavette, "An improved reconstruction procedure for the correction of local magnification effects in three-dimensional atom-probe," *Surface and Interface Analysis*, vol. 39, no. 2-3, pp. 268–272, 2007.

[7] B. Gault, D. Haley, F. de Geuser, M. P. Moody, E. A. Marquis, D. J. Larson, and B. P. Geiser, "Advances in the reconstruction of atom probe tomography data," *Ultramicroscopy*, vol. 111, no. 6, pp. 448–457, 2011.

[8] N. Rolland, F. Vurpillot, S. Duguay, B. Mazumder, J. S. Speck, and D. Blavette, "New atom probe tomography reconstruction algorithm for multilayered samples: Beyond the hemispherical constraint," *Microscopy and Microanalysis*, vol. 23, no. 2, p. 247–254, 2017.

[9] C. Hatzoglou, G. Da Costa, and F. Vurpillot, "Enhanced dynamic reconstruction for atom probe tomography," *Ultramicroscopy*, vol. 197, pp. 72–82, 2019.

[10] B. Gault, M. P. Moody, J. M. Cairney, and S. P. Ringer, *Tomographic Reconstruction*, pp. 157–209. New York, NY: Springer New York, 2012.

[11] A. Hegde, E. Weiss, W. Windl, H. Najm, and C. Safta, "Bayesian calibration with embedded model error for model diagnostics," *International Journal for Uncertainty Quantification*, 2023.

[12] A. Hegde, E. Weiss, W. Windl, H. Najm, and C. Safta, "Bayesian calibration of interatomic potentials for binary alloys," *Computational Materials Science*, vol. 214, p. 111660, 2022.

[13] F. Vurpillot and C. Oberdorfer, "Modeling atom probe tomography: A review," *Ultramicroscopy*, vol. 159, pp. 202–216, 2015.

[14] A. Moore, "The structure of atomically smooth spherical surfaces," *Journal of Physics and Chemistry of Solids*, vol. 23, no. 7, pp. 907–912, 1962.

DISTRIBUTION A: Distribution approved for public release.

[15] A. Suvorov and T. Razinkova, "Computer simulation of tungsten field evaporation by field-ion microscope," *Surface Science*, vol. 65, no. 1, pp. 354–360, 1977.

[16] D. Haley, M. P. Moody, and G. D. Smith, "Level set methods for modelling field evaporation in atom probe," *Microscopy and Microanalysis*, vol. 19, no. 6, p. 1709–1717, 2013.

[17] Z. Xu, D. Li, W. Xu, A. Devaraj, R. Colby, S. Thevuthasan, B. P. Geiser, and D. J. Larson, "Simulation of heterogeneous atom probe tip shapes evolution during field evaporation using a level set method and different evaporation models," *Computer Physics Communications*, vol. 189, pp. 106–113, 2015.

[18] C. Fletcher, M. P. Moody, and D. Haley, "Fast modelling of field evaporation in atom probe tomography using level set methods," *Journal of Physics D: Applied Physics*, vol. 52, p. 435305, aug 2019.

[19] C. Fletcher, M. P. Moody, and D. Haley, "Towards model-driven reconstruction in atom probe tomography," *Journal of Physics D: Applied Physics*, vol. 53, no. 47, p. 475303, 2020.

[20] C. Hatzoglou, B. Klaes, F. Delaroche, G. D. Costa, B. Geiser, M. Kühbach, P. B. Wells, and F. Vurpillot, "Mesoscopic modeling of field evaporation on atom probe tomography," *Journal of Physics D: Applied Physics*, vol. 56, p. 375301, jun 2023.

[21] M. Ashton, A. Mishra, J. Neugebauer, and C. Freysoldt, "Ab initio description of bond breaking in large electric fields," *Physical Review Letters*, vol. 124, no. 17, p. 176801, 2020.

[22] L. Yao, T. Withrow, O. D. Restrepo, W. Windl, and E. A. Marquis, "Effects of the local structure dependence of evaporation fields on field evaporation behavior," *Applied Physics Letters*, vol. 107, no. 24, p. 241602, 2015.

[23] C. G. Sánchez, A. Y. lozovoi, and A. alavi, "Field-evaporation from first-principles," *Molecular Physics*, vol. 102, no. 9-10, pp. 1045–1055, 2004.

[24] T. Ono, T. Sasaki, J. Otsuka, and K. Hirose, "First-principles study on field evaporation of surface atoms from w(011) and mo(011) surfaces," *Surface Science*, vol. 577, no. 1, pp. 42–46, 2005.

[25] J. Peralta, S. R. Broderick, and K. Rajan, "Mapping energetics of atom probe evaporation events through first principles calculations," *Ultramicroscopy*, vol. 132, pp. 143–151, 2013.

[26] M. Karahka and H. Kreuzer, "Field evaporation of oxides: A theoretical study," *Ultramicroscopy*, vol. 132, pp. 54–59, 2013. IFES 2012.

[27] X.-Y. Cui and S. P. Ringer, "On the nexus between atom probe microscopy and density functional theory simulations," *Materials Characterization*, vol. 146, pp. 347–358, 2018.

DISTRIBUTION A: Distribution approved for public release.

[28] C. Freysoldt, A. Mishra, M. Ashton, and J. Neugebauer, "Generalized dipole correction for charged surfaces in the repeated-slab approach," *Phys. Rev. B*, vol. 102, p. 045403, Jul 2020.

[29] T. Ohnuma, "First-Principles Calculation of the Evaporation Field and Roll-up Effect of M (M = Fe, Cu, Si, and Mn) on the Fe (001) and Fe Step Structure," *Microscopy and Microanalysis*, pp. 1–7, 2021. Publisher: Cambridge University Press.

[30] J. Dziedzic, A. Bhandari, L. Anton, C. Peng, J. C. Womack, M. Famili, D. Kramer, and C.-K. Skylaris, "Practical approach to large-scale electronic structure calculations in electrolyte solutions via continuum-embedded linear-scaling density functional theory," *The Journal of Physical Chemistry C*, vol. 124, no. 14, pp. 7860–7872, 2020.

[31] A. Nakata, D. R. Bowler, and T. Miyazaki, "Large-scale dft methods for calculations of materials with complex structures," *Journal of the Physical Society of Japan*, vol. 91, no. 9, p. 091011, 2022.

[32] L. Genovese, M. Ospici, T. Deutsch, J.-F. Méhaut, A. Neelov, and S. Goedecker, "Density functional theory calculation on many-cores hybrid central processing unit-graphic processing unit architectures," *The Journal of Chemical Physics*, vol. 131, p. 034103, 07 2009.

[33] C. Chang, V. L. Deringer, K. S. Katti, V. Van Speybroeck, and C. M. Wolverton, "Simulations in the era of exascale computing," *Nature Reviews Materials*, vol. 8, pp. 309–313, Feb 2023.

[34] E. W. Müller, "Field desorption," *Physical Review*, vol. 102, no. 3, pp. 618–624, 1956.

[35] M. K. Miller and R. G. Forbes, *Field Evaporation and Related Topics*, pp. 111–187. Boston, MA: Springer US, 2014.

[36] B. Gault, M. P. Moody, J. M. Cairney, and S. P. Ringer, *From Field Desorption Microscopy to Atom Probe Tomography*, pp. 29–68. New York, NY: Springer New York, 2012.

[37] R. Gomer, "Field desorption," *The Journal of Chemical Physics*, vol. 31, no. 2, pp. 341–345, 1959.

[38] T. T. Tsong, "Field ion image formation," *Surface Science*, vol. 70, no. 1, pp. 211–233, 1978.

[39] F. Vurpillot, A. Bostel, A. Menand, and D. Blavette, "Trajectories of field emitted ions in 3d atom-probe," *The European Physical Journal - Applied Physics*, vol. 6, no. 2, pp. 217–221, 1999.

DISTRIBUTION A: Distribution approved for public release.

[40] B. P. Geiser, D. J. Larson, S. Gerstl, D. Reinhard, T. F. Kelly, T. J. Prosa, and D. Olson, "A system for simulation of tip evolution under field evaporation," *Microscopy and Microanalysis*, vol. 15, no. S2, pp. 302–303, 2009.

[41] C. Oberdorfer, S. M. Eich, and G. Schmitz, "A full-scale simulation approach for atom probe tomography," *Ultramicroscopy*, vol. 128, pp. 55–67, 2013.

[42] C. Oberdorfer and G. Schmitz, "On the field evaporation behavior of dielectric materials in three-dimensional atom probe: A numeric simulation," *Microscopy and Microanalysis*, vol. 17, no. 1, pp. 15–25, 2011.

[43] N. Rolland, F. Vurpillot, S. Duguay, and D. Blavette, "A meshless algorithm to model field evaporation in atom probe tomography," *Microscopy and Microanalysis*, vol. 21, no. 6, pp. 1649–1656, 2015.

[44] M. Gruber, F. Vurpillot, A. Bostel, and B. Deconihout, "Field evaporation: A kinetic monte carlo approach on the influence of temperature," *Surface Science*, vol. 605, no. 23, pp. 2025–2031, 2011.

[45] F. Djurabekova, S. Parviainen, A. Pohjonen, and K. Nordlund, "Atomistic modeling of metal surfaces under electric fields: Direct coupling of electric fields to a molecular dynamics algorithm," *Physical Review E*, vol. 83, no. 2, p. 026704, 2011.

[46] S. Parviainen, F. Djurabekova, S. P. Fitzgerald, A. Ruzibaev, and K. Nordlund, "Atomistic simulations of field assisted evaporation in atom probe tomography," *Journal of Physics D: Applied Physics*, vol. 49, no. 4, p. 045302, 2015.

[47] C. Oberdorfer, T. Withrow, L. J. Yu, K. Fisher, E. A. Marquis, and W. Windl, "Influence of surface relaxation on solute atoms positioning within atom probe tomography reconstructions," *Materials Characterization*, vol. 146, pp. 324–335, 2018.

[48] M. Veske, A. Kyritsakis, K. Eimre, V. Zadin, A. Aabloo, and F. Djurabekova, "Dynamic coupling of a finite element solver to large-scale atomistic simulations," *Journal of Computational Physics*, vol. 367, pp. 279–294, 2018.

[49] S. Katnagallu, M. Dagan, S. Parviainen, A. Nematollahi, B. Grabowski, P. A. J. Bagot, N. Rolland, J. Neugebauer, D. Raabe, F. Vurpillot, M. P. Moody, and B. Gault, "Impact of local electrostatic field rearrangement on field ionization," *Journal of Physics D: Applied Physics*, vol. 51, no. 10, p. 105601, 2018.

[50] Marcelin, M. R., "Contribution à l´étude de la cinétique physico-chimique," *Ann. Phys.*, vol. 9, no. 3, pp. 120–231, 1915.

[51] J. Qi, C. Oberdorfer, E. A. Marquis, and W. Windl, "Origin of enhanced zone lines in field evaporation maps," *Scripta Materialia*, vol. 230, p. 115406, 2023.

DISTRIBUTION A: Distribution approved for public release.

[52] A. F. Voter, F. Montalenti, and T. C. Germann, "Extending the time scale in atomistic simulation of materials," *Annual Review of Materials Research*, vol. 32, no. 1, pp. 321–346, 2002.

[53] J. Qi, C. Oberdorfer, W. Windl, and E. A. Marquis, "Ab initio simulation of field evaporation," *Phys. Rev. Materials*, vol. 6, p. 093602, Sep 2022.

[54] "APT Software TAPSim." `https://www.imw.uni-stuttgart.de/mp/forschung/atom_probe_RD_center/software/`. Accessed: 2021-09-19.

[55] "LAMMPS Molecular Dynamics Simulator." `http://lammps.org`. Accessed: 2021-09-19.

[56] S. Plimpton, "Fast parallel algorithms for short-range molecular dynamics," *Journal of Computational Physics*, vol. 117, no. 1, pp. 1–19, 1995.

[57] R. A. van der Berg, P. W. M. Blom, J. F. M. Cillessen, and R. M. Wolf, "Field dependent permittivity in metal-semiconducting srtio3 schottky diodes," *Applied Physics Letters*, vol. 66, no. 6, pp. 697–699, 1995.

[58] V. Migunov, A. London, M. Farle, and R. E. Dunin-Borkowski, "Model-independent measurement of the charge density distribution along an fe atom probe needle using off-axis electron holography without mean inner potential effects," *Journal of Applied Physics*, vol. 117, no. 13, p. 134301, 2015.

[59] Y. Mishin, D. Farkas, M. J. Mehl, and D. A. Papaconstantopoulos, "Interatomic potentials for monoatomic metals from experimental data and ab initio calculations," *Phys. Rev. B*, vol. 59, pp. 3393–3407, Feb 1999.

[60] S. M. Foiles, "Calculation of the surface segregation of ni-cu alloys with the use of the embedded-atom method," *Phys. Rev. B*, vol. 32, pp. 7685–7693, Dec 1985.

[61] B. Onat and S. Durukanoğlu, "An optimized interatomic potential for cu–ni alloys with the embedded-atom method," *Journal of Physics: Condensed Matter*, vol. 26, p. 035404, dec 2013.

[62] C. Oberdorfer and W. Windl, "Bond-order bond energy model for alloys," *Acta Materialia*, vol. 179, pp. 406–413, 2019.

[63] R. Johnson, "Alloy models with the embedded-atom method," *Physical Review B*, vol. 39, no. 17, p. 12554, 1989.

[64] L. Ward, A. Agrawal, K. M. Flores, and W. Windl, "Rapid production of accurate embedded-atom method potentials for metal alloys," 2012.

[65] P. C. Roth, H. Shan, D. Riegner, N. Antolin, S. Sreepathi, L. Oliker, S. Williams, S. Moore, and W. Windl, "Performance analysis and optimization of the rampage metal alloy potential generation software," in *Proceedings of the 4th ACM SIGPLAN*

DISTRIBUTION A: Distribution approved for public release.

International Workshop on Software Engineering for Parallel Systems, SEPS 2017, (New York, NY, USA), p. 11–20, Association for Computing Machinery, 2017.

[66] M. K. Miller, *Field Ion Microscopy*, ch. 3, pp. 45–83. Boston, MA: Springer US, 2000.

[67] D. G. Ast and D. N. Seidman, "The field ion microscopy of gold," *Applied Physics Letters*, vol. 13, no. 10, pp. 348–350, 1968.

[68] Y. Muniandy, M. He, M. Eizadjou, E. P. George, J. J. Kruzic, S. P. Ringer, and B. Gludovatz, "Compositional variations in equiatomic crmnfeconi high-entropy alloys," *Materials Characterization*, vol. 180, p. 111437, 2021.

[69] B. Gault, M. P. Moody, J. M. Cairney, and S. P. Ringer, *Experimental protocols in atom probe tomography*, p. 150. New York, NY: Springer New York, 2012.

[70] M. Miller and M. Hetherington, "Local magnification effects in the atom probe," *Surface Science*, vol. 246, no. 1, pp. 442–449, 1991.

[71] M. Miller, "The development of atom probe field-ion microscopy," *Materials Characterization*, vol. 44, no. 1, pp. 11–27, 2000.

[72] L. Yao, "A filtering method to reveal crystalline patterns from atom probe microscopy desorption maps," *MethodsX*, vol. 3, pp. 268–273, 2016.

[73] A. R. Waugh, E. D. Boyes, and M. J. Southon, "Investigations of field evaporation with a field-desorption microscope," *Surface Science*, vol. 61, no. 1, pp. 109–142, 1976.

[74] A. F. Voter, "Hyperdynamics: Accelerated molecular dynamics of infrequent events," *Phys. Rev. Lett.*, vol. 78, pp. 3908–3911, May 1997.

[75] M.-C. Marinica, L. Ventelon, M. R. Gilbert, L. Proville, S. L. Dudarev, J. Marian, G. Bencteux, and F. Willaime, "Interatomic potentials for modelling radiation defects and dislocations in tungsten," *Journal of Physics: Condensed Matter*, vol. 25, p. 395502, sep 2013.

[76] C. Oberdorfer, S. M. Eich, M. Lütkemeyer, and G. Schmitz, "Applications of a versatile modelling approach to 3d atom probe simulations," *Ultramicroscopy*, vol. 159, pp. 184–194, 2015.

[77] C. Oberdorfer, *Numeric Simulation of Atom Probe Tomography*. PhD thesis, Westfälischen Wilhelms-Universität Münster, 2014.

[78] B. Gault, M. P. Moody, F. de Geuser, D. Haley, L. T. Stephenson, and S. P. Ringer, "Origin of the spatial resolution in atom probe microscopy," *Applied Physics Letters*, vol. 95, no. 3, p. 034103, 2009.

DISTRIBUTION A: Distribution approved for public release.

[79] B. Gault, M. P. Moody, F. De Geuser, A. La Fontaine, L. T. Stephenson, D. Haley, and S. P. Ringer, "Spatial resolution in atom probe tomography," *Microscopy and Microanalysis*, vol. 16, no. 1, p. 99–110, 2010.

[80] F. Vurpillot, S. Parviainen, F. Djurabekova, D. Zanuttini, and B. Gervais, "Simulation tools for atom probe tomography: A path for diagnosis and treatment of image degradation," *Materials Characterization*, vol. 146, pp. 336–346, 2018.

[81] B. Gault, M. Müller, A. La Fontaine, M. P. Moody, A. Shariq, A. Cerezo, S. P. Ringer, and G. D. W. Smith, "Influence of surface migration on the spatial resolution of pulsed laser atom probe tomography," *Journal of Applied Physics*, vol. 108, no. 4, p. 044904, 2010.

[82] A. R. Waugh, E. D. Boyes, and M. J. Southon, "Field-desorption microscopy and the atom probe," *Nature*, vol. 253, no. 5490, pp. 342–343, 1975.

[83] A. Cerezo, D. Gibuoin, S. Kim, S. Sijbrandij, F. Venker, P. Warren, J. Wilde, and G. Smith, "Materials applications of an advanced 3-dimensional atom probe," *JOURNAL DE PHYSIQUE IV*, vol. 6, pp. 205–210, SEP 1996. 43rd International Field Emission Symposium (IFES96), MOSCOW, RUSSIA, JUL 14-19, 1996.

[84] W. Lefebvre, A. Loiseau, and A. Menand, "Field evaporation behaviour in the γ phase in ti–al during analysis in the tomographic atom probe," *Ultramicroscopy*, vol. 92, no. 2, pp. 77–87, 2002.

[85] T. Boll, T. Al-Kassab, Y. Yuan, and Z. Liu, "Investigation of the site occupation of atoms in pure and doped tial/ti3al intermetallic," *Ultramicroscopy*, vol. 107, no. 9, pp. 796–801, 2007.

[86] J. Wesemann, G. Frommeyer, and M. Kreuss, "Apfim investigations on ordered γ-tial using single-layer detection method," *Applied Surface Science*, vol. 87-88, pp. 179–184, 1995. Proceedings of the 41st International Field Emission Symposium.

[87] S. Kim and G. Smith, "Ap-fim investigation on γ-based titanium aluminides," *Materials Science and Engineering: A*, vol. 239-240, pp. 229–234, 1997. 4th Conference on High-Temperature Intermetallics.

[88] T. Boll and T. Al-Kassab, "Interpretation of atom probe tomography data for the intermetallic TiAl+Nb by means of field evaporation simulation," *Ultramicroscopy*, vol. 124, pp. 1–5, 2013.

[89] R. R. Zope and Y. Mishin, "Interatomic potentials for atomistic simulations of the ti-al system," *Phys. Rev. B*, vol. 68, p. 024102, Jul 2003.

[90] E. A. Marquis and F. Vurpillot, "Chromatic aberrations in the field evaporation behavior of small precipitates," *Microscopy and Microanalysis*, vol. 14, no. 6, p. 561–570, 2008.

DISTRIBUTION A: Distribution approved for public release.

[91] A. Biswas, D. J. Siegel, C. Wolverton, and D. N. Seidman, "Precipitates in al–cu alloys revisited: Atom-probe tomographic experiments and first-principles calculations of compositional evolution and interfacial segregation," *Acta Materialia*, vol. 59, no. 15, pp. 6187–6204, 2011.

[92] M. Takeda, Y. Maeda, A. Yoshida, K. Yabuta, S. Konuma, and T. Endo, "Discontinuity of g.p.(i) zone and θ'-phase in an al-cu alloy," *Scripta Materialia*, vol. 41, no. 6, pp. 643–649, 1999.

[93] F. Apostol and Y. Mishin, "Interatomic potential for the al-cu system," *Phys. Rev. B*, vol. 83, p. 054116, Feb 2011.

[94] Y. Mishin, M. Mehl, and D. Papaconstantopoulos, "Phase stability in the fe–ni system: Investigation by first-principles calculations and atomistic simulations," *Acta Materialia*, vol. 53, no. 15, pp. 4029–4041, 2005.

[95] Y. Mishin and A. Lozovoi, "Angular-dependent interatomic potential for tantalum," *Acta Materialia*, vol. 54, no. 19, pp. 5013–5026, 2006.

[96] X.-Y. Liu, C.-L. Liu, and L. Borucki, "A new investigation of copper's role in enhancing al–cu interconnect electromigration resistance from an atomistic view," *Acta Materialia*, vol. 47, no. 11, pp. 3227–3231, 1999.

[97] A. Bigot, F. Danoix, P. Auger, D. Blavette, and A. Menand, "3d reconstruction and analysis of gp zones in al-1.7cu (at%): a tomographic atom probe investigation," *Applied Surface Science*, vol. 94-95, pp. 261–266, 1996. Proceedings of the 42nd International Field Emission Symposium.

[98] D. Beinke, C. Oberdorfer, and G. Schmitz, "Towards an accurate volume reconstruction in atom probe tomography," *Ultramicroscopy*, vol. 165, pp. 34–41, 2016.

[99] O. S. Center, "Ohio supercomputer center," 1987.

DISTRIBUTION A: Distribution approved for public release.